OPTO-MECHANICAL MANIPULATION OF MOLECULES AND CHEMICAL REACTIONS

A Dissertation

Presented to the Faculty of the Graduate School

of Cornell University

In Partial Fulfillment of the Requirements for the Degree of

Doctor of Philosophy

by

Xavier Serey

August 2013

OPTO-MECHANICAL MANIPULATION OF MOLECULES AND CHEMICAL REACTIONS

Xavier Serey, Ph. D.

Cornell University 2013

We developed optical methods to manipulate molecules in a microfluidic environment. Optical tweezers can manipulate micro-spheres in solutions with the gradient force but are not practical for spheres smaller than 500 nm in diameter. Nanotweezers use the evanescent field out of waveguides, slot-waveguides, plasmonic resonances, and photonic crystal resonators. They were able to manipulate objects down to 40 nm. Proteins and many biomolecules are of sizes on the order of a few nanometers, *a priori* out of reach of these techniques. During my PhD, I developed nanophotonic and nano-optic systems aimed at applying electromagnetic potential wells to bias the motion of molecules against Brownian motion and eventually demonstrated that chemical reaction pathways could also be altered. I showed that photonic crystal resonators are a toolbox for nanoscale assembly enabling trapping, transport, and orientation of nano-objects. I also investigated the heat arising in optofluidic photonic crystals and found it to be higher than previously thought, up to 57 K for 10 mW of power input, which makes such devices incompatible with biological single molecule experiments. I then used electromagnetic fields shaped by waveguides-carbon nanotubes hybrids to trap immunoglobulin of mass down to 160 kDa. Last, I developed the optical manipulation of chemical reactions. I showed that

electromagnetic gradient force can transport molecules across reaction barriers along a reaction coordinate demonstrating it experimentally by guiding the adsorption of immunoglobulin proteins onto carbon nanotubes. These techniques are part of a wider evolution that is changing the way we interact with molecules. Although originally dismissed for studying single molecules because of the diffraction limit, nano-optics and nanophotonics are becoming the center of this revolution.

BIOGRAPHICAL SKETCH

Xavier Serey defended his PhD thesis at Cornell University in July 2013 on optical manipulation of molecules. He had been a PhD student in the School of Applied and Engineering Physics since 2009, he joined the Erickson Lab to work on trapping with photonic crystals. In reverse chronological order, his work focused on experimental demonstration of opto-mechanical chemistry, optical trapping of various molecules and objects, clean room nano-fabrication, and theoretical modeling of nanophotonic devices for trapping. Prior to his PhD, Xavier earned a Diplôme d'Ingénieur from École Centrale Paris and studied Physics and Mathematics. Before, he prepared for the entrance examination at Lycée Fénelon Sainte-Marie.

Pour Patricia et François

ACKNOWLEDGMENTS

I have many persons to thank for making my PhD such a good time, Faculty and Staff, colleagues, friends, and the Ithacan community. Never-ending winters, warm summers, and short springs were all great not least thanks to all of them. Really, the autumn in this place needed no one to be enjoyable, but their presence made it truly tremendous.

I first want to thank my advisor, David Erickson, for his guidance and advice. I am extermelygrateful for his efforts in providing feedback on my ideas, in keeping his cool every time I went off on a tangent, in providing me with enough funding, and for all of his other forms of support throughout my PhD.

I would also like to thank Camil Muscalu and Alexander Gaeta for doing me the honor of being in my committee. I want to thank Prof. Muscalu for the many hours he spent chatting with me, these were always instructional and enjoyable. Prof. Gaeta taught the first class I took in Cornell, and I am glad he will be in the audience for my Defense. Among the outstanding Faculty, I am also particularly grateful to Piet Brouwer, Tung-Mow Yan, David Muller, Manfred Lindau, Peng Chen, and Roald Hoffmann for discussions, recommendation letters, advice, supervision, and teaching.

The staff at Cornell and in the CNF was also helpful all along and I thank in particular Patti Wojcik, Erin Burke, Marcia Sawyer, Derek Stewart, Steven Johnson, and Daron Weslty.

I enjoyed working with my colleagues, particularly Sudeep Mandal and Yih-Fan Chen who taught me research and whose successes I tried to imitate, Pilgyu Kang, with

whom I had the pleasure of closely collaborating, and Dakota O'Dell who made transferring my knowledge seem easy and fun. I also enjoyed many conversations and friendships with the other lab members: Bernardo, Allen, Mekala, Michael K., Aram, Sean, Erica, Michael M., Abdullah, Matt, Aadhar, Vlad, Li, Saad, Seoho, and Perry.

Naming all the close friends that made my stay in Ithaca a blast is a tricky exercise, I'll try nevertheless: Laitage, Shawn, Rafael, Jakub, Michael (again), Guy, Antoine, Raphaël, Nick, Lei, Erica, Nithin, and Charlie. In the broader Cornell and Ithaca community I also want to thank the CCC and the SA for welcoming me. I owe a great debt to Eliana Para who first welcomed me in Ithaca and saw I didn't lack of anything.

My girlfriend, Mo Chen, was the most supportive person during my PhD, she helped, encouraged, counseled me and spiced up my life these past few years. This thesis is a piece of our lives. My family is a constant source of inspiration. My grand-parents were a motivation in trying to become a scientist. My siblings, Carolina and Pablo-Alain, challenge me and remind me there is an outside world. My parents, Patricia and François, provided me with the support, comfort, and encouragement, I know at what price. To them, to my mom in particular, I owe the greatest debt and gratitude, beyond what I can express.

Ithaca, NY,

July 2013

TABLE OF CONTENTS

LIST OF FIGURES

LIST OF TABLES

LIST OF ABBREVIATIONS

CNF Cornell Nanoscale Facility

CNT Carbon NanoTube

DLVO Debye Landau Verwey-Overbeek

FRET Förster Resonance Energy Transfer

Ig ImmunoGlobulin

MD Microcavity Design

MG Modegap Design

MH Microcavity plus Hole design

MT MicroTubule

NBTC NanoBioTechnology Center

PBS Phosphate Buffered Saline

PC Photonic Crystal

LIST OF SYMBOLS

E_A activation energy

ω angular frequency

c concentration

J current density

λ_D Debye length

ρ density

ρ_c density of charges

D diffusion coefficient

E electric field

k electromagnetic propagation constant

F Faraday number

R gas constant

Gr Grashof number

g gravitational acceleration

A Hamaker constant

δ Kronecker symbol

β longitudinal component of the k-vector

B magnetic field

$\overline{\overline{T}}$ Maxwell stress tensor

∇ nabla operator

NA numerical aperture

V_{eff} mode volume

μ_0 permeability of vacuum

ε_0 permittivity of vacuum

α polarizability

U_p potential energy

Q quality factor

Ra Rayleigh number

n refractive index of medium

ε relative permittivity

c speed of light in vacuum

κ spring constant (chapter 4)

S stability factor

S_T Soret coefficient

γ surface potential

T temperature

κ thermal conductivity (chapter 5)

D_T thermophoretic coefficient

T torque (chapter 4)

k_i trapping stiffness along direction i.

u, **v** velocities

η viscosity

λ wavelength

CHAPTER 1

INTRODUCTION

1.1 Background

Our ways to interact with molecules are changing rapidly. Despite high hopes set by science fiction, molecules were initially largely ignored by the revolution of nanotechnology, the most impactful achievements were in the field of material science and physics with the developments of microscopy methods allowing for the observation of atoms in materials and electronic orbital[1]. The major change in chemistry initiated during the past century came from the development of computational techniques allowing for the in-depth study of molecules and their interactions. This development, with the progress in the theoretical understanding of chemical mixtures and of the link between single events and ensemble measurements, has brought a renewed curiosity towards the study of single molecules.

In the past twenty years, new methods have been developed to interact with molecules in finer detail therefore providing chemists with new instruments that allow for precision measurements that were unimaginable until now. Among others, researchers have been interested in the detection of single molecules with Surface Enhanced Raman Spectroscopy[2], in measuring the conductivity of single molecules and single molecule electronics[3], in understanding their fluorescence properties[4], in implementing force spectroscopy on large molecules and biomolecules[5, 6], as well as measurements of vibrational spectroscopy[7]. Chemical reactions involving one molecule at a time have also drawn the interest of scientists[8]. In 2013, two ground

breaking papers involving novel ways to interact with molecules were published. An experimental verification of a theoretical proposal [9] that demonstrated the possibility to manipulate the spectroscopic selection rules in carbon nanotubes by exciting quadrupolar electronic transitions[10]. In 2013 as well, a new method to measure the Raman signal of a single molecule with sub-nanometer resolution was implemented by Zhang *et. al*[11] now allowing to visualize a molecule on a substrate in vacuum and its bonds with a resolution below a nanometer.

The latest method is particularly interesting as it is the result of new developments in nano-optics and nanofabrication. These new photonics, which development was supported by advances in nanofabrication, have proved false the idea that photons were not a suitable wave to explore nanoscale objects because of the diffraction limit. The development of nano-cavities and other nanoscale resonant devices have greatly contributed to creating electromagnetic fields with high k-vectors in one direction which is a major requirement for confining the electromagnetic field to small regions[12]. The progress in engineering fields is bound to lead to numerous applications in molecular optics.

The literature often informally distinguishes two approaches to nanoscale electromagnetism that have attracted most attention: the one using fields shaped by refractive indices alone, usually referred to as nanophotonics, and the one making use of metals or resonances in molecules, referred to as nano-optics. As mentioned above, the development of these systems is the result of newly largely available methods for nanofabrication. Appendix A displays a schematic view of a typical fabrication procedure for a photonics chip. Since these methods were originally developed for the

electronics industry, similar materials as in the electronics industry have been used so far. By far the most common material is silicon and its derivatives. The influence of the telecommunication industry has also led to a large adoption of 1550 nm as a working wavelength, although not optimal *a priori* for obtaining high k-vector components.

1.2 Scientific Contributions

The behaviour of molecules in solution is governed by energy barriers, potential wells, and stochastic events. In particular, chemical reactions are often described in terms of a reaction energy diagram along a reaction coordinate. The research presented in this thesis describes my efforts towards applying electromagnetic potential wells to bias the motion of molecules against Brownian motion and eventually demonstrate that reaction pathways could also be altered. The resulting effect, that we called "opto-mechanical chemistry", represents a novel approach to reaction engineering.

1.2.1 Manipulation of molecules in solution

Traditional optical tweezers are diffraction limited and do not allow for the trapping of particles below 500 nm without high power usage that can damage the samples. The trapping force exerted on a particle depends on the gradient of the electric field intensity and on the radius cube of the particle which shows the extreme difficulty in scaling optical tweezers to smaller objects. Instead, researchers have developed nanophotonic and nano-optics approaches to trapping where fields are confined to sub diffraction limited volumes.

In the chapter 3, I developed theoretically photonic crystal designs aimed at trapping smaller objects. I showed that inserting a central hole allows to increase the trapping force on small molecules. The method was experimentally demonstrated in two publications[13, 14]. In the chapter 4, I demonstrated that these devices could also be used to control the orientation of nano-rods. These devices therefore allowed to control 5 out of 6 of the degrees of freedoms of these solid rods.

1.2.2 Behavior of molecules in the vicinity of a Photonic Crystal

Nanoscale optofluidic resonators have proven useful in fields ranging from chemical and biological sensing [15] to nano-manipulation [16, 17]. Most nanophotonic devices were operating at 1550 nm as mentioned above, a wavelength at which water absorbs particularly well as visible in Fig. 1. The temperatures reached in these devices had not been characterized and the effects of heat on transport of solutes had not been studied. Transport is critical in nanophotonics, because as the size of the electromagnetic hotspot diminishes the likelihood of a molecule being transported into the field decreases.

In the chapter 5, I found, experimentally and numerically, that the temperature increase in optofluidic photonic crystals could be as high as 57K for 10mW of input power. The resulting optical trapping and biomolecular sensing properties of these devices are affected by the resulting combination of buoyancy driven flow and thermophoresis. Specifically, the region around the electromagnetic hotspot is depleted in biomolecules because of a high free energy barrier. This realization led to

the development of photonic crystal traps operating at lower wavelength were water absorbs less[13].

FIGURE. 1.1. Absorption of electromagnetic radiation of liquid water. Image credits: Wikimedia commons.

Chapter 6 presents some of the methods that were developed for this study. It was partly published as supplementary information to the journal article "DNA Delivery and Transport in Thermal gradients near Optofluidic Resonators".

1.2.3 Molecules in a chemical reaction

In energetic terms, reactions are described by energy diagrams that reflect the change in potential along an abstractly defined reaction coordinate. Valleys and hills in this plot represent stable states, reaction intermediary states, and activation energies. Figure 2 displays an example of a reaction diagram.

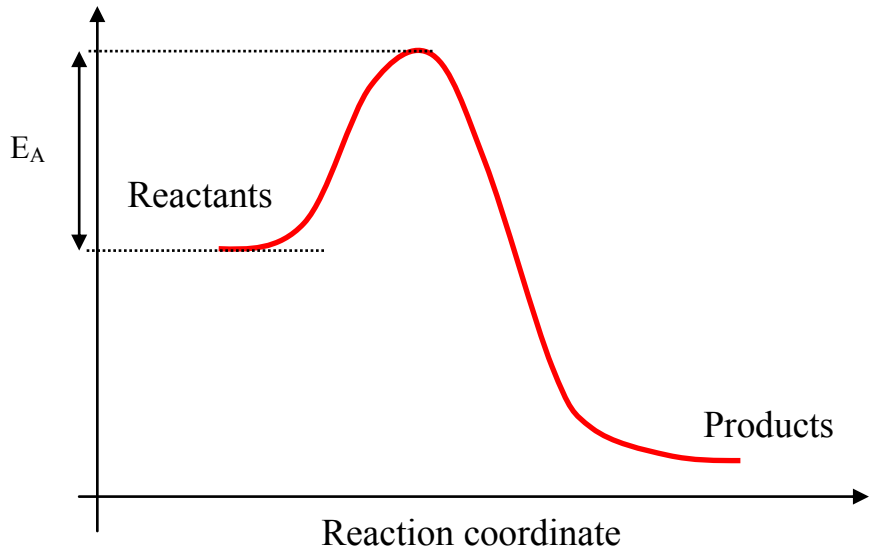

FIGURE 1.2. Schematic of a one step reaction energy diagram.

To overcome the energy barrier, several strategies have been developed that rely on either modifying the energy diagram by introducing reaction intermediaries, or by providing the energy in bulk, most often as kinetic energy. The first method relies on trial and error finding a suitable catalyst able to fasten a desired reaction. Numerical simulations, intuition, and trial and error are the most common methods for finding a suitable catalyst. The second method is more intuitive and easier to implement but suffers from a lack of specificity. The energy provided to the reactants can help them overcome the desired energy barrier but will also help them overcome other energy barriers along other coordinates, thus driving undesired reactions which could overall lower the reaction efficiency.

In the chapter 7, I demonstrate a novel technique where electromagnetic potential energy is applied along a reaction coordinate to favor a reaction. The model reaction is the surface adsorption of immunoglobulin proteins onto carbon nanotubes.

1.2.4 List of publications

In the course of my PhD, I have taken part in work leading to seven publications, three of which were as first author, one as co-first author, and three as second author. Here is the list:

1. Serey, Xavier, O'Dell, Dakota, Kang, Pilgyu, Erickson, David, "Opto-Mechanical Chemistry" In preparation (2013).

2. Kang*, Pilgyu, Serey*, Xavier, Chen, Yih-Fan, Erickson, David, "Angular Orientation of Nanorods Using Nanophotonic Tweezers" Nano Letters, (2012). * co-first author.

3. Chen, Yih-Fan, Serey, Xavier, Erickson, David, "Controlled photonic manipulation of proteins and other nanomaterials" Nano Letters 12 (3), 1633-1637 (2012).

4. Serey, Xavier, Mandal, Sudeep, Chen, Yih-Fan, Erickson, David, "DNA Delivery and Transport in Thermal gradients near opto-fluidic resonators" Physical Review Letters, 108, 048102 (2012).

5. Erickson, David,Serey, Xavier, Chen, Yih-Fan, Mandal, Sudeep, Nanomanipulation using near field photonics" Lab on Chip, 11, 995-1009 (2011), Cover article.

6. Serey, Xavier, Mandal, Sudeep, Erickson, David, "Comparison of silicon photonic crystal resonator designs for optical trapping of nanomaterials" Nanotechnology, 21, 305202 (2010).

7. Mandal, Sudeep,Serey, Xavier, Erickson, David, "Nanomanipulation using Silicon Photonic Crystal Resonators" Nano Letters 10, 99-104 (2010).

1.3 Future vision

The broader impact of this work lies in developing new means to interact with molecules. It is aimed at allowing for the manipulation of molecules as building blocks and provide all fields of science and engineering with an intuitive method that resembles the way we interact with macroscopic objects. For example with otpo-mechanical chemistry, assembling two molecules is no longer the result of random collisions and chance but is a process of bringing them together in a controlled manner similarly to what is done at higher scales.

The methods developed are part of a set of tools that are becoming available to scientists and engineers to better understand, and use molecules. The control over five of six degrees of freedom of a nanorod in a solution was achieved and molecules of molecular weight down to 160 kDa were manipulated. Heat represents a major challenge in the operation of optofluidic devices but its effect can be mitigated by strategies as demonstrated by Wang *et al.*[18]. Precise engineering of the nanophotonic and nano-optical elements should allow for a better heat dissipation and trapping of smaller molecules. Appendix B presents a proposed strategy to mitigate heat in photonic-plasmonic hybrids inspired by their strategy that could potentially allow for the trapping of molecules down to 1.6 kDa.

Another challenge that remains is parallelization for processing. The single molecules have proven to allow for a precise observation and manipulation of molecules. When competing with traditional chemistry, they have a serious lack in quantity. In the current paradigm, their practical use is limited to applications where a small number of

events are desired, enough for certain applications such as biophysical studies or assembly of nano-objects, but not for large scale processing.

CHAPTER 2

NECESSARY BACKGROUND

In this chapter, I will extremely briefly introduce some of the concepts that are reused throughout the thesis. Despite this, some familiarity with optics, electromagnetism and fluid dynamics will be necessary.

2.1 Maxwell's equations and Poynting's theorem of conservation of momentum

Although buried under several layers of sophistication in modern optics, I could not start my dissertation any other way than reminding the reader of Maxwell's beautiful equations for electromagnetic fields.

$$\vec{\nabla} \cdot \vec{E} = \frac{\rho_c}{\varepsilon_0} \tag{2.1}$$

$$\vec{\nabla} \cdot \vec{B} = 0 \tag{2.2}$$

$$\vec{\nabla} \times \vec{E} = -\frac{\partial \vec{B}}{\partial t} \tag{2.3}$$

$$\vec{\nabla} \times \vec{B} = \mu_0 \left(\vec{J} + \varepsilon_0 \frac{\partial \vec{B}}{\partial t} \right) \tag{2.4}$$

In these equations, $\boldsymbol{E}$ is the electric field, ρ_c is the charge density, ε_0 is the permittivity of vacuum, $\boldsymbol{B}$ is the magnetic field, μ_0 is the permeability of vacuum, and $\boldsymbol{J}$ is the current density. This is also an appropriate opportunity to point out that I will use SI units in this chapter while the paper chapters (chapter 3 and onwards) were redacted in Gaussian units.

We ignored here the derivations that lead to the Maxwell's equations from the free field Lagrangian. It is therefore suitable to ignore the derivations leading to Poynting's theorem of conservation of momentum. The equation for the conservation of momentum links the change in momentum of objects $\boldsymbol{P}_{mech}$ and of the electromagnetic field $\boldsymbol{P}_{field}$ to the Maxwell stress tensor $\overline{\overline{T}}$. It reads:

$$\frac{d}{dt}\left(\vec{P}_{field}+\vec{P}_{mech}\right)=\oiint\overline{\overline{T}}\cdot\vec{n}\,dS \tag{2.5}$$

$$\vec{P}_{field}=\mu_0\varepsilon_0\iiint_V\vec{E}\times\vec{B}\,d^3x=\iiint_V\vec{g}\,d^3x \tag{2.6}$$

$$T_{\alpha,\beta}=\varepsilon_0\left[E_\alpha E_\beta+c^2B_\alpha B_\beta-\frac{1}{2}\left(\vec{E}\cdot\vec{E}+c^2\vec{B}\cdot\vec{B}\right)\delta_{\alpha,\beta}\right] \tag{2.7}$$

In these equations, we defined $\boldsymbol{g}$, which we recognize to be the electromagnetic momentum density, and used the Kronecker delta, δ, in the tensor definition of the Maxwell stress tensor.

The definition of $\boldsymbol{g}$ shows that electromagnetic waves carry momentum that is proportional to their Poynting vector with a proportionality coefficient of $1/c^2$. The Poynting vector being the direction of the energy flow, we therefore recognize that photons carry momentum along their direction of propagation, or k-vector. This is the conceptual starting point of the work presented here: Engineering ways of exchanging this momentum between the light and objects through equation (2.5) and exploring the physics that arise.

2.2 Optical trapping

2.2.1 Brief History of Optical Trapping

Optical trapping is a technique taking advantage of the transfer of momentum between photons and objects in their path. It was pioneered by Arthur Ashkin, and quickly found numerous applications in physics and biology.

In condensed matter physics for example, expansions of the technique were celebrated by a Nobel Prize attributed to Steven Chu, and are now a common element of most labs studying low temperature atomic condensates. In biophysics, the group of Steven Block first took advantage of optical tweezers for single molecule studies. Optical tweezers are now a ubiquitous tool in the single molecule communities and have been perfected to reveal very fine details in the interaction of molecules.

2.2.2 Radiation pressure

The radiation pressure is the force that photons can exert on a surface upon being reflected, diffracted, or absorbed. Schematically, the trajectory of a light beam in air going through non absorbing bead (of refractive index 1.59) is the following:

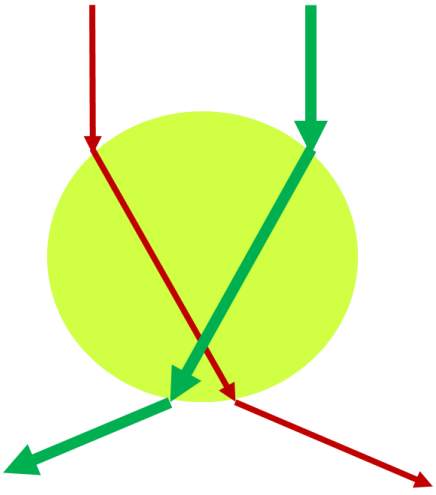

FIGURE. 2.1. Light beams going through a polystyrene bead.

Because the momentum of the beam is directed in the direction of propagation, the change in direction of propagation (that results from Snell-Descartes' laws of refraction) must be counterbalanced by a change in momentum of the bead as seen in Equation (2.5). If the left and right beams are of the same intensity, the two exchanges in momentum compensate in the transverse direction leading to a net force only along the axial direction, it is called the scattering force. If they do not compensate, the net transfer in momentum will also have a component along the transverse direction directed towards the regions of highest electromagnetic intensity, it is called the gradient force. The gradient force is the force used in optical tweezers, it is proportional to the polarizability, α, of an object or a molecule through the formula (letting aside all derivations):

$$\vec{F}_{grad} = \frac{\alpha}{2}\vec{\nabla}E^2 \tag{2.8}$$

The polarizability of molecules is roughly proportional to their mass, and therefore loosely proportional to their volume. For solid objects defined by a refractive index, one needs to calculate the polarizability by calculating the net field (imposed field and depolarization field) around the object. For a spherical particle much smaller than the wavelength, this calculation leads to the well known expression:

$$\vec{F}_{grad} = \frac{n_m}{2}\frac{n_p - n_m}{n_p + 2n_m} r^3 \vec{\nabla}E^2 \tag{2.9}$$

Where n_m and n_p are the refractive indices of the medium and sphere respectively, and r is the radius of the sphere.

The above equations show the difficulty of trapping smaller objects as the force exerted decreases linearly with the mass of the object. This expression also motivates

the strategy for producing higher trapping forces: creating fields that decay on a shorter scale such that the gradient term in (2.8) increases.

2.3 Waveguides and Photonic Crystals

2.3.1 Dielectric Waveguides

The case of a light beam between two dielectric slabs allows for an intuitive explanation of dielectric waveguides. They are geometries where light is permanently confined and guided along a direction. The confinement mechanism in the case of a slab waveguide presented in Fig. 2.2. is the total internal reflection at each interface.

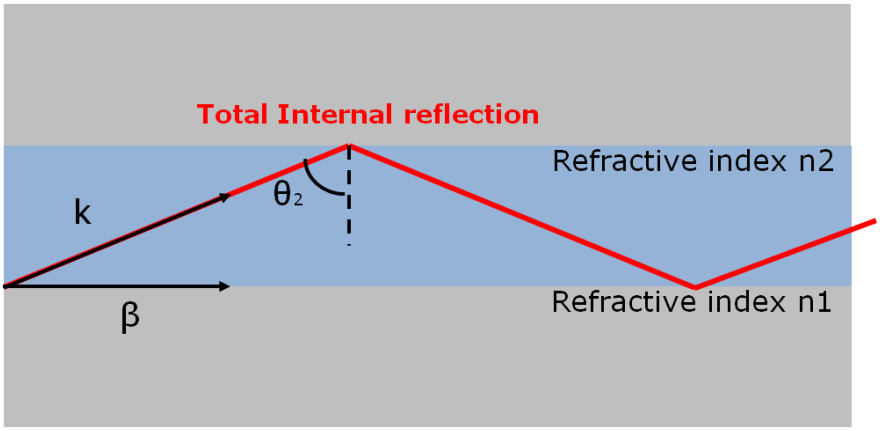

FIGURE. 2.2. Total internal reflection in a slab waveguide.

If the angle θ_2 of the incident light ray satisfies the relation $\frac{n_2}{n_1}\sin(\theta_2) > 1$, the light is totally reflected because no outgoing angle can satisfy Snell-Descartes' law. If the two slabs are parallel, this reflection will happen with the same angle at each interface and the light will be confined in the internal medium and guided in the horizontal direction.

Mathematically, guided modes can be seen as an eigenvalue problem. Light in a medium propagates following the wave equation for the electric field:

$$\left(\left(\frac{c}{n}\right)^2 \nabla^2 - \frac{\partial^2}{\partial t^2}\right)\vec{E} = 0 \tag{2.10}$$

Where c is the speed of light in the vacuum. A guided mode along the z direction can be defined as an eigenvalue solution to the Helmholtz equation, which is obtained plugging the ersatz solution $\vec{E}(\vec{r},t) = \mathrm{Re}\{\vec{E}(x,y)e^{-i\omega t - i\beta z}\}$ in (2.10). It is a statement of invariance in the z direction. The equation reads:

$$\Delta_\perp{}^2 \vec{E}(x,y) + \left(\left(\frac{\omega}{c}\right)^2 n(x,y)^2 - \beta^2\right)\vec{E}(x,y) = 0 \tag{2.11}$$

where β is the longitudinal component of the k-vector. Numerical solvers are the best way to find geometries that allow for guided modes. Fig. 2.3 presents the field distribution obtained numerically for a rectangular geometry and the SEM image of its experimental realization. It is composed of a rectangular beam of Silicon (refractive index 3.47 at 1550 nm) on top of silicon dioxide (refractive index 1.45).

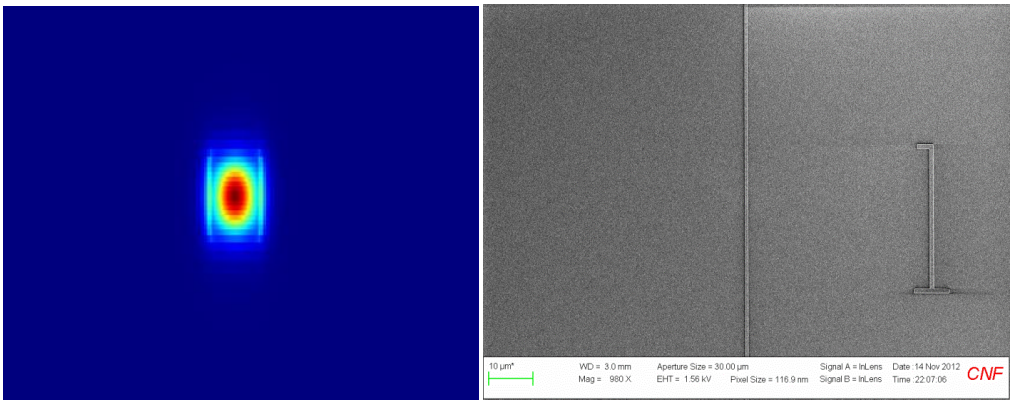

FIGURE. 2.3. Numerical simulation of a guided mode (slab view) and SEM image of the realization of the same waveguide.

2.3.2 Photonic Crystals

Photonic crystals are periodic arrangements of dielectric materials. Some photonic crystals have the useful property of completely reflecting or transmitting a small range of frequencies (they act as mirrors for the frequencies that they do not transmit).

As I am not aware of any short yet complete introduction to the topic, this chapter will only contain essential facts and intuition.

Let's consider the case of a period of *L* along the x direction. Because the solution to (2.10) must have the same periodicity as the medium, Floquet and later Bloch showed that they must have the form $\vec{E}(\vec{r},t) = \vec{E}_{k_x}(\vec{r},t)e^{-ik_x x}$ with $k_x \in (0, 2\pi/L]$ and $\mathbf{E_{kx}}$ also has period L. This form of solution is essentially the same as the ersatz used to establish (2.11) but where $k_x \in (0,\infty)$ because the continuous symmetry can be seen as the case were $L \longrightarrow \infty$ and the z dependence removed for the same reason.

A first important consequences of the general Bloch theorem (which extends Floquet's solution to 3D) is that the k-vector only needs to be evaluated in a particular region called the Brillouin zone (in the 1D example, this region was $(0, 2\pi/L]$ but it is more complex in the general case). Another consequence is that since the exponential term modifies the phase of the wave but not its amplitude, hence waves are transmitted through photonic crystals without deformation. In 1D, the mode profile at any x-plane of a photonic crystal therefore gives enough information to determine it elsewhere in the crystal. In particular, as we will see, if no mode is found, an incident wave must be completely reflected within a few periods of the surface of the crystal as it will not be allowed to exist in the crystal.

The case of the Bragg reflector can provide some intuition on why a mode could be disallowed in the photonic crystal. The Bragg reflector is the layered superposition of two materials with different refractive indices as seen in Fig. 2.4 where only one layer is shown.

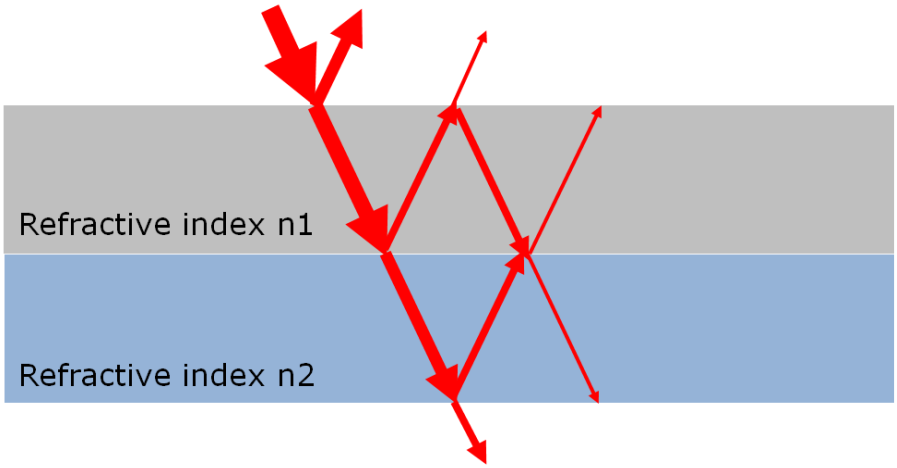

FIGURE. 2.4. Bragg reflector. For simplicity, the angles were not drawn to respect Snell-Descartes' laws of refraction.

At each interface light can be transmitted or reflected (according to the transmission and reflection coefficients of the interface at the angle of incidence). While propagating through the mediums, the light gains a phase shift $\varphi = 2\pi n L/\lambda$, with L the travelled path in the material of index n, and λ the wavelength in vacuum. If the phase shift difference between light having undergone an even number of reflections is an odd multiple of π, the intensity on the output side of the reflector will be small which translates into having only a small amount of light transmitted through the reflector. If the construct of Fig. 2.4 is to be repeated, the periodic arrangement would nullify the frequencies that undergo deconstructive interference.

2.4 Flow in microfluidics

2.4.1 Navier Stokes equation

For an incompressible Newtonian fluid, the Navier-Stokes equation describes the fluid flow in terms of the velocity of a fluid element. It reads:

$$\rho\left(\frac{\partial v}{\partial t}+\left(\vec{v}\cdot\nabla\right)\vec{v}\right)=-\vec{\nabla}p+\eta\nabla^2\vec{v}+\vec{f} \tag{2.12}$$

Where $\boldsymbol{v}$ is the velocity, p is the pressure, η the viscosity, and $\boldsymbol{f}$ represents volumetric forces.

2.4.2 Microfluidics

Several dimensionless numbers are associated with the Navier Stokes equation, to evaluate compare different physics of the flow. The Reynolds number $\mathrm{Re}=\rho vL/\eta$ compares inertial forces to viscous forces. In the case of microfluidics, it is extremely small which indicates the inertial terms (left handside) of the Navier Stokes equation will be negligible, the simplified equation for microfluidics reads:

$$-\vec{\nabla}p+\eta\nabla^2\vec{v}+\vec{f}=0 \tag{2.13}$$

2.4.3 Boussinesq approximation

Buoyancy occurs when the density of the medium is higher than that of its surroundings. Temperature, for example, can locally change the density of the fluid which induces buoyancy. In order to include this effect without using a compressible version of the Navier Stokes equation, Boussinesq introduced the following volume force to the equation:

$$\vec{f}=-\vec{g}\left(\rho\left(T\right)-\rho\left(T_0\right)\right) \tag{2.14}$$

Where **g** is the gravitational acceleration vector, and T is the temperature.

2.5Transport of molecules in solution

In solution, in the absence of energy potentials, molecules undergo diffusion through a process called Brownian motion. The diffusion can be related to the displacement of the molecule through the formula:

$$\sqrt{\langle x^2 \rangle} = 2\sqrt{Dt} \tag{2.15}$$

Where x is the time dependent coordinate along one degree of freedom, D is the diffusion coefficient and t is time. The Einstein relation specified the relation of the diffusion coefficient to the size of a spherical object:

$$D = \frac{k_B T}{6\pi\eta r} \tag{2.16}$$

With k_B the Boltzmann constant. This relation indicates that the smaller an object, the broader the Brownian motion it will undergo therefore making its observation difficult and its manipulation more challenging. The Einstein relation is valid for translational degrees of freedom but a similar equation exists for rotational degrees of freedom confirming the same trend. These equations motivate the necessity of developing tools to control molecules against thermal fluctuations.

2.5.1 Convection diffusion

Equation (2.15) is obtained from the pure diffusion equation. Often times, other physical forces will modify the diffusion equation and affect the transport of molecules in solution. In microfluidics, it is necessary to take into account the fluid flow that can exist in the channel. The velocity profile of the molecules, ***u***, is usually

considered for simplicity to be that of the flow **v** from (2.13) (an assumption gradually false when considering smaller molecules) which is obtained from the incompressible Navier Stokes equation. Adding the contribution of the convective flux to the diffusion equation, in the case of microfluidics one obtains for the concentration *c*:

$$\frac{\partial c}{\partial t} = D\nabla^2 c - \vec{u} \cdot \vec{\nabla} c \tag{2.14}$$

With the notations previously defined.

2.5.2 Thermophoresis

Another physical effect that can affect the motion of molecules is the presence of a temperature gradient. Experimentally, the migration of molecules towards the cooler zones was the first observed by Tyndall. Rayleigh explained this effect in gases while Soret explained it in liquids. In colloids however, it was discovered that the effects can be much more complicated and the diffusion can go into the warm regions. The driving mechanisms are still being researched and discussed.

For the purpose of evaluating diffusion, the most useful expression of thermophoretic migration is the one that relates the speed of the migration to the temperature gradient:

$$\vec{u_T} = -D_T \vec{\nabla} T \tag{2.15}$$

In this equation $\boldsymbol{u_T}$ is the thermophoretic velocity, and D_T is the thermophoretic coefficient which hides the complex physics at play. It is useful to us because with this correction to the velocity of the particles in solution, we can re-write the convection diffusion equation to account for thermodiffusion:

$$\frac{\partial c}{\partial t} = D\nabla^2 c - \vec{\nabla} \cdot \left(c \left(\vec{u} - D_T \vec{\nabla} T \right) \right) \tag{2.16}$$

With the same notations as in (2.14) and (2.15).

CHAPTER 3

COMPARISON OF SILICON PHOTONIC CRYSTAL RESONATOR DESIGNS FOR OPTICAL TRAPPING OF NANOMATERIALS

3.1 Abstract

The use of silicon photonic devices for optical manipulation has recently enabled the direct handling of objects like nucleic acids and nanoparticles that are much smaller than could previously be trapped using traditional laser tweezers. The ability to manipulate even smaller matter however requires the development of photonic structures with even stronger trapping potentials. In this work we investigate theoretically several photonic crystal resonator designs and characterize the achievable trapping stiffness and trapping potential depth (sometimes referred to as trapping stability. Two effects are shown to increase these trapping parameters: field enhancement in the resonator and strong field containment. We find trapping stiffness as high as 22.3 pN nm^{-1} for 100nm polystyrene beads as well as potential depth of 51000 k_BT at T=300K per Watt of power input to the bus waveguide. Under the same conditions for 70nm polystyrene beads, we find a stiffness of 69 pN nm^{-1} and a potential depth of 177000 k_BT. Our calculations suggest that with input powers of 10mW we could trap particles as small as 7.7nm diameter with a trapping depth of 500 k_BT. We expect these traps could eventually enable the manipulation of small matter such as single proteins, carbon nanotubes and metallic nanoparticles.

Reprinted with permission from Serey *et al.*, and the Institute of Physics, "Comparison of Silicon Photonic Crystal Resonators Designs for Optical Trapping of Nanomaterials", Nanotechnology, 21, 305202 (2010).

3.2. Introduction

Since the original experiments reported in Ashkin's founding article [1], optical or laser tweezing techniques [2] have been used in a large number of different areas including: single cell dynamics [3], optical chromatography [4, 5], directed assembly [6, 7], and have already helped understand complex phenomena like cellular motility [**8**] and single DNA mechanical properties [9]. Though extremely successful at these size scales a limitation of traditional optical tweezers is in manipulating smaller dielectric objects, on the order of 100nm or less. A few optical tweezing techniques have been developed to trap nanoscopic objects [10, 11] but not generally pure dielectrics which are closer approximations to biological species. From Rayleigh theory it is well known that the optical gradient force, which is usually exploited as the trapping force in optical tweezers, scales with the radius of the particle cubed [12]. Roughly speaking then, it takes a 1000 fold increase in the applied trapping power to apply the same force to a particle that is only 10 times smaller.

In order to overcome this limitation a number of new, near field optical manipulation techniques have been developed which exploit the strong forces that can be generated in the near field of plasmonic or resonant photonic structures. These devices, recent variations of which include plasmonic tweezer [13, 14, 15], whispering gallery mode carousel [16] and photonic crystal resonators [17, 18, 19], have the added benefit of also being in a format which can be readily integrated with a lab-on-chip device while exploiting the enhanced field provided by photonic resonances. Further improvements in these devices have recently been introduced by allowing the full strength field

directly interact with the trapped particle using either slot and hole apertures [17, 18, 20, 21]. Using the photonic crystal resonator, we have been able to evanescently trap particles as small as 48nm in diameter [19]. The experimentally demonstrated state of the art technique in terms of high trapping stiffness is provided by the Self Induced Back Action design trapping 50nm particles with a stiffness of the order of 7 pN nm^{-1} W^{-1}.

With the aim of being able to optically manipulate even smaller material, we explore theoretically the trapping potential of a number of silicon photonic crystal resonator designs and evaluate them against techniques such as those described above. In the devices we examine here, the resonators are excited through evanescent coupling from a bus waveguide (figure 3.1) as this offers the greatest multiplexing possibilities and is in line with what we have demonstrated experimentally [22]. To the best of our knowledge it is the first time comprehensive calculations are performed with resonant devices to evaluate the trapping stiffness and stability. It is essential to perform comprehensive calculations since the Rayleigh approximation does not hold for the same range of particle sizes in tightly confined electromagnetic fields. The sizes of the particles considered in this work are in the limit of the Rayleigh approximation range. In our devices, the perturbative approach is also affected by the inaccuracy of the Clausius-Mossotti polarizability in fields with high gradients. In a previous work, Barth *et al*. [17] performed exact calculation to estimate the dependence of resonant traps on the size of the trapped bead. Recently, Lin *et al.* [18] performed perturbative calculations to estimate the trapping capacity. In this paper, we present an exact approach to the stiffness evaluation while addressing the issues arising from the

resonant wavelength shift that Barth *et al.* predicted by taking great care to distinguish the numerical impact and the physical contribution.

In the first two sections of this paper, we introduce the three devices we focused on, namely the microcavity design (MD), the mode-gap design (MG), and the microcavity plus hole design (MH), and then the details of the numerical analysis method used to characterize them. After that we present and discuss the results in sections 3.5 and 3.6 focusing on the MH design because it offers the highest stiffness and stability. Tables in section 3.5 provide direct comparison of these results with the state of the art.

3.3. System description

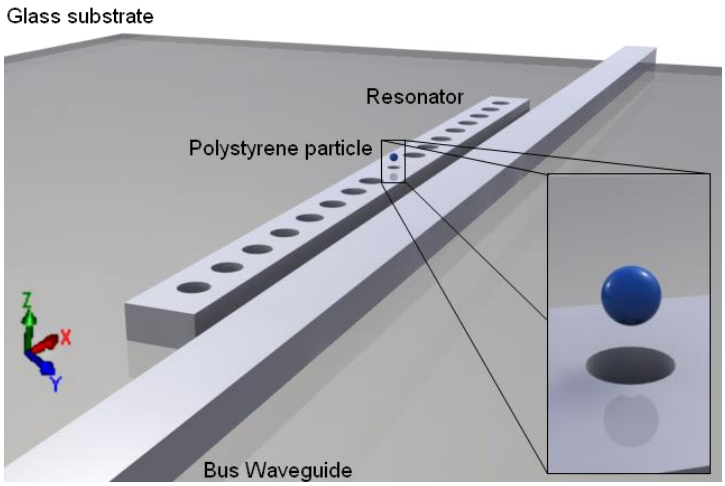

FIGURE 3.1. Evanescently coupled linear resonator for optical trapping. In this study we investigated three resonator designs including the "microcavity plus hole" (MH) design shown here. The trapped particle is shown above the central hole.

Optical resonators are devices in which photons travel along a closed path. Fabry-Pérot resonators represent a class of resonator in which light bounces back and forth between two facing mirrors. In such a cavity, the allowed modes are those where the

different light rays constructively interfere with each others. The resonant condition is given by the constructive interference condition that the phase delay in the resonator should be an integer multiple of 2π. In photonic crystal resonators, the cavity is sandwiched between two photonic crystal mirrors, thus presenting a newer version of the Fabry Pérot resonator (figure 3.1). The sub diffraction limited field confinement allows for higher gradients. According to the Rayleigh theory, the trapping force is proportional to the gradient of E^2 [12]. Hence we obtain higher forces with tighter field confinement. The stable position is located at the maximum of the field. In their movement, the particles will preferably follow the streamlines of the gradient of E^2 towards the stable position.

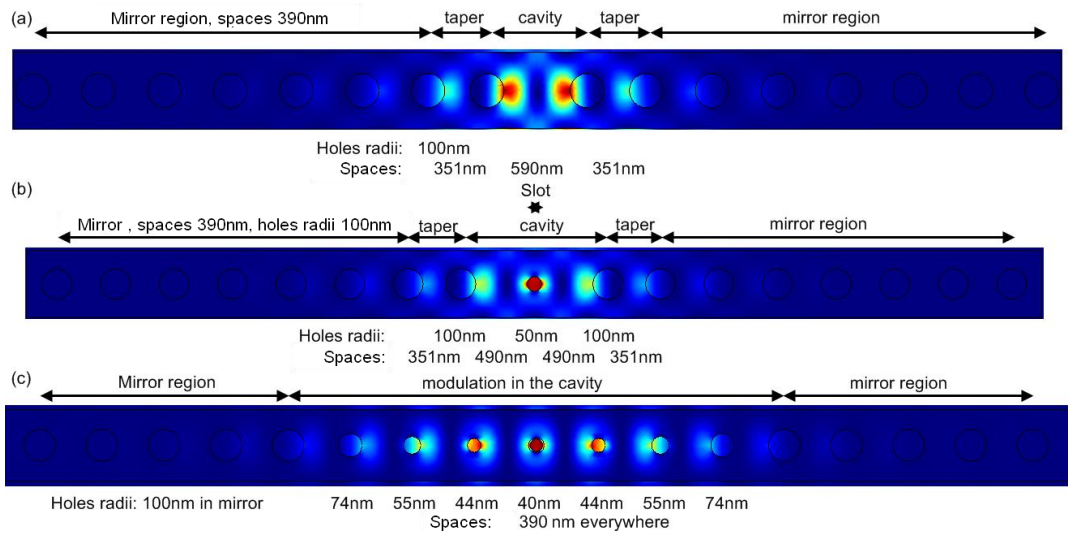

FIGURE 3.2. Specifications for the three photonic crystal resonator devices investigated here showing the computed electric field at resonance. (a) The Microcavity design, (b) the Microcavity plus Hole design, and (c) and the ModeGap design. In all figures, the spaces refers to the centre-to centre distance between the holes. The core photonic crystal was chosen such that it acts as a mirror for 1550nm wavelength light.

In figure 3.2, we present the three photonic crystal resonator designs examined here, which we refer to herein as: the micro-cavity design (MD), the mode gap design (MG), and the microcavity plus hole design (MH). All the resonator devices presented here were assumed to have the bulk properties of silicon (refractive index $n_{silicon}$=3.47) and had cross-sectional dimensions of 250nm high by 450 nm wide. As shown in figure 3.1, light was coupled into the resonators evanescently from another silicon bus waveguide (also 250nm height per 450 nm large) which ran alongside the resonator. The devices lie on a silica substrate (n_{glass}=1.45), mimicking a device fabricated from a silicon-on-insulator wafer, and the surrounding medium is assumed to be water (n_{water}=1.33). The MD design (figure 3.2a) consists of two identical tapered Bragg mirrors [23]. Each reflector comprises of 7 holes of radius 100 nm separated by a lattice constant a=390 nm. An eighth hole at distance 0.9*a is added and serves as a taper. The microcavity itself has a total length of 1.5*a. As in the MD device, the MH device is an implementation of Velha *et al.*'s [23] design for high quality factor 1D photonic crystals. The MH device and the MD are very similar, with the difference being that an additional 50 nm radius hole is placed at the centre of the cavity region. It serves as an inner cavity in which light the intensity will be increased, the effect is clearly visible in figure 3.2b, which is exposed to the liquid state for trapping. At any liquid/silicon boundary, the field is increased because of boundary conditions and then vanishes as an evanescent wave. The superposition of these evanescent waves in the inner cavity hole is what allows for the formation of this high field intensity region. The MG design is inspired from mode-gap photonic crystal resonators, which have recently been demonstrated to exhibit very high quality factors. The MG design

(figure 3.2c) consists of a standard periodic photonic crystal (same lattice constant a) where the radius of the etched holes varies from 100 nm at the edges to 40 nm at the centre.

3.4. Details of Numerical Analysis

The numerical technique we used here consisted of repeatedly computing the trapping forces while shifting the particle's physical position along one of the main axes (figure 3.1). The force was estimated through the Maxwell stress tensor [24] given a geometrical frame and its related refractive indices list. The simulations performed here were done using a commercial finite element code (COMSOL). The finite element method, FEM, was preferred over a finite difference time domain, FDTD, technique due to much lower time memory requirements. The long photon residence time in the high quality factor optical resonators necessarily results in an extremely long simulation time in order to accurately compute the fields and forces using an FDTD method. A drawback was that wavelength-dependant estimations required several FEM simulations whereas one FDTD simulation would have sufficed. For the calculation of wavelength dependant quantities below, we parameterised the simulation and solved for wavelengths spanning the resonant domain. The Q factor is an example of a wavelength dependant quantity, which was approximated here via Eq. (3.1).

$$Q \approx \frac{\lambda_r}{\Delta\lambda} \tag{3.1}$$

In this formula, knowledge of λ_r the resonant wavelength and of $\Delta\lambda$ the full width at half maximum is required.

The main objective of the simulations was to predict the trapping capabilities of the three designs discussed above. In all cases the trapping forces were computed by including a polystyrene bead ($n_{polystyrene}$=1.59) in the computational domain and then integrating the Maxwell stress tensor over an artificial boundary region that included the particle.

$$\vec{F}_{EM} = \oint \overline{\overline{T}}_{Maxwell} \cdot \vec{n} dS \tag{2}$$

In this expression $\boldsymbol{F}_{EM}$ is the electromagnetic force, $\boldsymbol{T}_{Maxwell}$ is the Maxwell stress tensor and $\boldsymbol{n}$ is the outgoing vector normal to the surface. In our simulations, the integration surface was a sphere 10 nm bigger in radius than the particle itself. We verified that changing the integration surface did not affect significantly the computed force.

A number of mesh quality experiments were conducted in order to ensure convergence of the solution. Generally speaking, higher mesh qualities were required in the region of the particle and integrating sphere in order to obtain the expected resonance condition and convergence of the force value. We found that the simulation's meshing affected the numerical resonant wavelength. This alteration was not physical and was disregarded by ensuring the resonant condition in all simulations. For higher *Q* factors or larger particle sizes, the particle's position would have a sufficiently pronounced effect on the resonant wavelength that it could significantly alter the trapping conditions. We describe in the end of section 3.6 how, in cases where this resonance

shift is important, this can become a practical advantage by making the wavelength a tuneable trapping element.

From the force calculations, we were able to extract two parameters commonly used to describe optical traps: the trapping stability [12] and the trapping stiffness [25]. To do this, we start the calculation from the stable position, which is the equilibrium point, and move the particle away from it repeating the force computation at every point. For distances not too far from the equilibrium point, the force response is similar to a linear spring where the spring constant is equal to the trapping stiffness. The trapping stiffness therefore, is the derivative of the restoring force with respect to the position perturbation around the equilibrium point as described by Eq. (3).

$$k_i = \left(\frac{\partial F_i}{\partial X_i} \right)_{equilibrium} \tag{3}$$

In this equation, k_i and F_i are the stiffness and force in the direction parameterised by X_i. These values are computed for 1W of laser power into the bus waveguide, we use the units per Watt to lift this dependence as all of the numbers we present are proportional to the input power. The trapping stiffness can be evaluated along the three coordinate axes with the lowest result representing the limiting one. Hence we refer to it as the effective stiffness. The harmonic approximation also allows us to express the mean displacement of the particle when trapped in the potential. We can express the mean deviation $<x^2>$ using the equipartition theorem:

$$k\left\langle x^2 \right\rangle = k_B T \tag{4}$$

Where k is the effective stiffness of the trap –i.e. the stiffness in the weakest direction– , x is the displacement along one direction, k_B is the Boltzmann constant and T is the temperature in Kelvin.

The other parameter is of interest here is the trapping stability, which is related to the likelihood of the random thermal energy being able to free the particle from the trap. The stability leads to the average trapping time proportional to its exponential following a Kramers escape process [26] . It is defined as the ratio of the potential energy depth to the available thermal energy as shown in eq. (5).

$$S = \frac{W}{k_B T} \tag{5}$$

Here, W the work necessary to bring the particle from a free position to the stable point for 1W of pumping power to the waveguide, k_B and T were already introduced in equation 4. The potential energy is equal to the opposite of the work necessary to bring the particle from a free position to the equilibrium trapped position. In accordance with analytical expectations [27], we used an exponential interpolation of the decaying force profile as the particle rises away from the resonator in the evanescent field to compute the release work W.

3.5. Results

3.5.1 *Particles larger than the diameter of the central cavity hole*

Using the simulation methods described above, we evaluated the trapping characteristics of the three designs described above. In table 3.1 we report the

trapping stiffnesses along all three coordinate axes and maximum force, for the MD, MH and MG devices as described in section 3.3. As can be seen the MH design exhibited the highest stiffness and thus we will expand on that here as an illustrative case. Figure 3.3 illustrates the electric field and force profiles computed as described above. For a 100 nm particle, the trapping stiffnesses for the MH design were found to be 22.3 pN nm^{-1} W^{-1} and 37.5 pN nm^{-1} W^{-1} in the X and Y directions respectively. The X and Y stiffnesses were calculated for a particle which bottom was positioned 20 nm above the resonator surface with a 1W of laser power input into the bus waveguide. The stable position of the MH resonator coincided with the centre of the device. The electric field is polarized in the Y direction; hence boundary discontinuity conditions induce a higher gradient along that axis accounting for the larger stiffness value. Along the Z-axis (figure 3.3d), an exponential decay in the force profile was obtained which is consistent with the evanescent nature of the field outside the resonator. The decay length, the inverse of the argument in the exponential, was 50 nm and the calculated stiffness was 65.5 pN nm^{-1} W^{-1}. Therefore the effective stiffness of the MH design is 22.3 pN nm^{-1} W^{-1}.

TABLE 3.1. Calculated stiffness' for MD, MG and MH designs for 100 nm particle.

Resonator Design	Microcavity Design (MD)	Mode Gap Design (MG)	Microcavity plus hole (MH)
X – direction Stiffness (pN nm^{-1} W^{-1})	4.81	13.1	22.3
Y – direction Stiffness (pN nm^{-1} W^{-1})	3.30	14.0	37.5
Z – direction Stiffness (pN nm^{-1} W^{-1})	8.53	31.3	65.5
Effective Stiffness (pN nm^{-1} W^{-1})	3.30	13.1	22.3
Maximum force (pN W^{-1})	700	2070	4100
Q factor	500	1400	2200

Stiffness' are the result of the linear interpolation of the F_{Xi} vs X_i curve around the equilibrium point of the device. When compared with the state of the art devices described in the introduction, the MH device yields stiffness' and stability values significantly higher than other tweezers. In table 3.2, we have tabulated reported stiffnesses from recently published articles and compared them to the results obtained here. The SIBA tweezer, which reports the highest published stiffness to date, offers a 8.2pN $nm^{-1}W^{-1}$ effective stiffness for 100nm polystyrene (n=1.575) [21]. It uses the optical resonance of a light wave propagating through a small aperture. When a particle is present in the aperture, it induces a shift in the resonance. By illuminating

the aperture with a detuned wavelength, the particle induces the resonance. It is the fact that the resonance is sensitive in the position of the particle that allows such high stiffness. The maximum force remains of the order of 250 pN W^{-1} for a 100nm particle [21]. The resonant nanotweezer described here can offer forces as high as 4.1 nN W^{-1}. This can be compared to the typical force exerted by the evanescent field of a waveguide which is of the order of 1 pN W^{-1}.

TABLE 3.2. Comparison of stiffness' for several trapping devices recently published.

Device	Trapped particle, size (nm)	Trapping Stiffness (pN nm^{-1} W^{-1})
Microcavity design (MD)	Polystyrene, 100	3.30
	Polystyrene, 200	7.93
Mode gap design (MG)	Polystyrene, 100	13.1
	Polystyrene, 200	26.85
Microcavity plus hole (MH)	Polystyrene, 100	22.3
Self induced back action [21]	Polystyrene, 100	8.2
	Polystyrene, 50	6.6
Slot waveguides [20]	Polystyrene, 100	0.2
Plasmonic tweezer [14]	Polystyrene, 200	0.013
Conventional tweezer [28]	Polystyrene, 220	0.027
Standing Gaussian Wave [29]	Polystyrene, 100	1

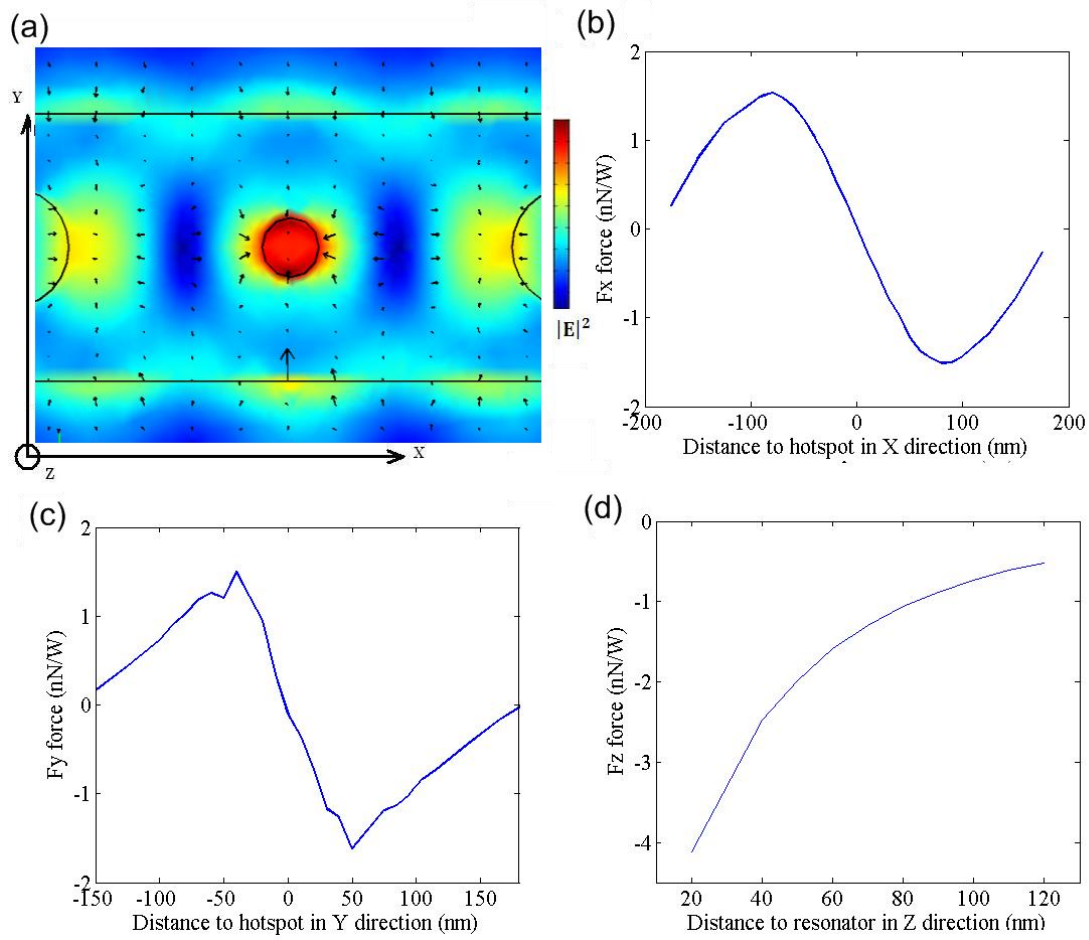

FIGURE 3.3. Numerical results for the microcavity plus hole (MH) device. (a) Field intensity and its gradient (arrow plot) when the MH trapping design is on resonance without a particle in the simulation domain. (b,c) Force profiles for the particle as it is moved along the resonator (X axis) and across the resonator (Y axis). In all simulations the particle was maintained at a vertical height of 20 nm above the resonator. (d) Z-axis force profile computed as the particle is maintained above the resonator's centre and moved from 20nm to 120nm above top plane of the device. The stiffnesses were evaluated using linear interpolation around the stable position. In the X and Y directions (b,c) the linear approximation is very accurate. In the Z direction (c), we did not take the slope at Z=20nm but also linearly interpolated the data between 20 and 80nm which is a conservative estimate. (b,c,d) All calculations done for a polystyrene bead (n=1.59) with a diameter of 100nm.

As alluded to above, the stability factor is the ratio of the work required to remove the particle from the trap, to the random thermal energy in the system. Very stable traps therefore have S>>1, and unstable traps have S<1. We calculated the potential energy

of the trap by integrating the work needed to release the particle from 20nm above the resonator's centre to a distance far away from it such that the particle no longer feels the trapping force. In order to be consistent with the rest of the data, we have calculated the work to extract the particle from a position 20nm above the resonator. The results for all three designs presented here are shown in table 3.3. As can be seen, the trapping stabilities as high as 44000 W^{-1} were obtained for the MH design. In table 3.3, we also note that the decay length (defined as the inverse of the argument in the exponential in the force expression) for the force in the Z direction decreases when the stability factor increases suggesting that the increased gradient over compensated for the slightly shorter distance over which the force was applied. As with the previous case the stability factors were found using a 100 nm polystyrene particle as a model target.

TABLE 3.3. Trapping Stability for a 100nm diameter polystyrene bead.

Trapping Method	Stability factor at 300K (W^{-1})	Decay length (nm)
Microcavity design (MD)	9000	60
Mode gap design (MG)	26000	55
Microcavity plus hole (MH)	44000	50
Slot waveguides, 65nm diameter particle [30]	875	50 – 100

3.5.2 *Particles smaller than the hole diameter*

Unlike the previous cases for 100nm particles, for the MH and MG devices, the most stable position for trapped smaller particles is within the central cavity hole rather than resting on top of the device. The hole walls offer physical confinement in the X and Y directions and thus stiffnesses along these axes are no longer relevant. For these smaller particles, we therefore studied the forces along the Z-axis position while remaining inside the hole. It has already been outlined that for this type of devices [18] the position of a large particle within the hole can affect the resonance. Our simulations confirmed that for a 70nm polystyrene particle in the central hole of the MH resonator, the resonant wavelength is shifted by 0.4nm, which is consistent with the results presented by Lin *et al.* [18]. For a 40 nm test particle, the resonant wavelength shift was lower than that resolvable by the solution and thus not considered in the simulations. We used a mesh cladding cylinder around the central hole in order to overcome the numerical errors that the shift in the particle's position caused. This "mesh cladding" served as a shield to the mesh perturbation caused by the changing position of the particle inside the hole.

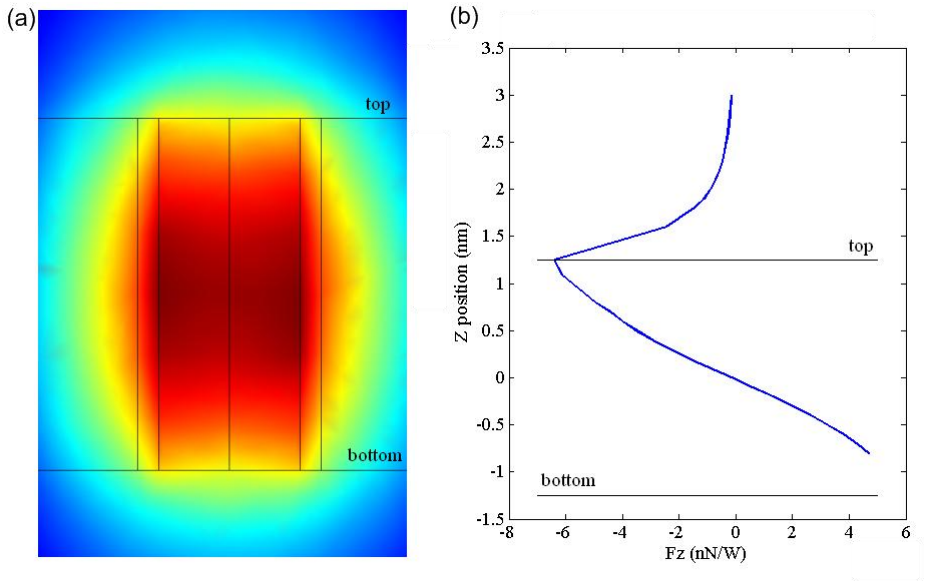

FIGURE 3.4. Field and force in the central hole. (a) Representation of E in the central hole in a plane along the resonator. (b) Trapping force in the central hole for a 70nm polystyrene particle. The Z position represents the position of the centre of the particle. The Z axes in (a) and (b) are not to scale for clarity purposes.

For each position of the particle, we set the wavelength to match the new resonance. As we explain in section 3.6, the average displacement is small enough that the local variations in the resonant wavelength are negligible. For the 70nm and 40nm polystyrene particles, we summarized the calculated stiffnesses and stabilities in table 3.4. The forces calculation used for the 70nm case are plotted in figure 3.4. Because of the enhanced interaction with the field in the hole, the resulting forces are much greater than those for larger particles evanescently trapped. The 11 pN nm^{-1} W^{-1} stiffness we report for a 40 nm particle compares to SIBA's 7.2 pN nm^{-1} W^{-1} for a 50nm particle [21]. The highest stiffness we report here is that for a 70nm particle which is 69 pN nm^{-1} W^{-1}. In addition to these stiffnesses, in table 4 we also report the inferred stability number for the SIBA design from the reported trapping energy [21]. Such high figures of merit in both cases are the result of the enhanced field-particle

interaction that occurs within the hole in this case, or the hole in the metal sheet for the SIBA design.

TABLE 3.4. Stiffness', and stabilities for smaller particles.

Device	Trapped particle, size (nm)	Trapping Stiffness (pN nm^{-1} W^{-1})	Stability (W^{-1})
Microcavity plus hole (MH)	Polystyrene, 70	69	177000
	Polystyrene, 40	11	70000
Self induced back action [21]	Polystyrene, 50	6.6	
Standing Gaussian wave [11]	DVB n= 1.592, 50	0.06	

3.6. Discussion

The quest for particle tweezers with higher trapping stiffness and stabilities is justified by the desire to efficiently trap and manipulate smaller molecules and other nanomaterials. In this paper, we explore the possibility of higher stiffness' and forces than what has been previously published. We see from equation 4 that higher trapping stiffness results in better confinement and therefore greater certainty in the particles position. Therefore achieving high trapping stiffness is a necessary step towards handling smaller molecules. For a 100nm particle and a 10mW power input, the best design we developed (the MH design) yields the particle's position uncertainty as

$<x^2>^{1/2}$=4.3nm. For the 70nm and the 40nm particles, and 10mW of input power, the particle's position uncertainties are respectively 2.45nm and 6.1nm. Over these distances, the resonant wavelength shift is minor. When considering smaller spherical particles, we can use the Rayleigh theory to compute the expected forces, in this case the force varies proportionally to the volume of the particle [12]. With this approach we can derive the following two relations:

$$\left(\frac{D}{40}\right)^{3/2} = \frac{6.1}{\left\langle x^2 \right\rangle^{1/2}} \tag{6}$$

$$S = 700 \times \left(\frac{D}{40}\right)^3 \tag{7}$$

Where D is the diameter of the Rayleigh particle in nanometers, $<x^2>^{1/2}$ and S are the standard deviation on the particle's position and its stability number under a 10mW of power input. Using the previous relations, we determine the smallest size of a spherical particle allowing for stable trapping (S>5), while having a standard deviation smaller than the hole height ($<x^2>^{1/2}$<250nm) to be 7.7nm leading to a stability number of 5 and a standard deviation of 72nm. In these cases, the variation in the resonant wavelength due to the random motion of a trapped particle is expected to be small in comparison with the line width of the resonator and not likely to "kick" the system out of resonance.

Increasing the trapping parameters is important in order to reduce the power requirements of the trap and by extension the degree of local heating. The most immediate way is through field enhancement (for a constant 1W of input power). The

force is proportional to the number of photons stored in the cavity which is proportional to the Finesse. Therefore a way of increasing the trapping force is building devices with higher *Q* factors, if the field profile remains similar. One has to be careful when using resonators with higher *Q* factors as the linewidth is smaller and the presence of a particle is more likely to kick the resonator out of resonance. This is well known by the biosensing community which uses ultra high *Q* factors to make very precise sensors [16, 31].

Among the exciting possibilities of these devices are those offered by the dependence of the resonant wavelength on the particle's position, in particular it's depth within the cavity hole. With these resonators it is possible to conceive of a power free optical trap by slightly red detuning the excitation from the resonant wavelength when no particle is in the cavity. If properly detuned, when a trapped particle begins to diffuse out of the cavity, it could force the system back into resonance applying a restoring force pushing the particle back into the trap. A particle trapped in the resulting arrangement would not experience any force unless it tries to leave the trap creating an effective optical cage. This leads to a trap with an effective stable volume rather than a stable point. This represents a new type of self induced trapping mechanism.

3.7. Conclusion

In this paper, our goal was to illustrate the possibilities offered by integrated optics for the trapping and manipulation of nanoscopic matter. We have evaluated three photonic crystal resonator designs and performed a theoretical study of their specifications as photonic traps. Our calculations indicate an important enhancement of the trapping parameters as compared to the state of the art. In the device offering the best performance, we find stiffness' as high as 22.3 pN nm^{-1} W^{-1} for a 100nm polystyrene particle, compared with the previously highest reported stiffness of 8.2 pN nm^{-1} W^{-1}. For smaller beads, the field particle interaction is increased in the central hole leading to increased trapping stiffness's. For a 70nm particle, we found the stiffness to be 69 pN nm^{-1} W^{-1} to be compared to 6.6 pN nm^{-1} W^{-1} previously reported for 50nm beads. The confinement in the central hole offers a greatly increased trapping stability with numbers as high as 177000 per Watt for a 70nm particle and 70000 for a 40nm particle. For particles down to 7.7nm size, we expect 0.08 pN nm^{-1} W^{-1} stiffness and stability as high as 500 W^{-1}. We also highlighted the difficulties and possibilities offered by the use of higher Q factors resonators. Increasing the Q factor increases the forces but also the resonant wavelength shift of the device. It opens some exciting possibilities such as self induced trapping.

3.8 Acknowledgements

This work was supported by the Nanobiotechnology Center (NBTC), an STC Program of the National Science Foundation under Agreement No. ECS-9876771, the National Institutes of Health - National Institute of Biomedical Imaging and Bioengineering (NIH-NIBIB) under grant number R21EB007031 and the US National Science Foundation – CAREER program through grant number 0846489.

REFERENCES

[1] Ashkin A, “Acceleration and Trapping of Particles by Radiation Pressure”, *Phys. Rev. Lett.*, **24**, 156 (1970).

[2] Neuman K C, and Block S M, “Optical trapping”, *Rev. Sci. Instrum.*, **75**, 2787-2809 (2004).

[3] Collin D, Ritort F, Jarzynski C, Smith S B, Tinoco Jr. I, and Bustamante C, “Verification of the Crooks fluctuation theorem and recovery of RNA folding free energies”, *Nature*, **437**, 231-234 (2005).

[4] Imasaka T, “Optical chromatography. A new tool for separation of particles”, *Analusis*, **26**, M53-M55 (1998).

[5] Terray A, Arnold J, and Hart S J, “Enhanced optical chromatography in a PDMS microfluidic system”, *Opt. Express*, **13**, 10406-10415 (2005).

[6] Agarwal R, Ladavac K, Roichman Y, Yu G, Lieber C, and Grier D, "Manipulation and assembly of nanowires with holographic optical traps", *Opt. Express*, **13**, 8906-8912 (2005).

[7] Jamshidi A, Pauzauskie P J, Schuck P J, Ohta A T, Chiou P Y, Chou J, Yang P, and Wu M C, “Dynamic manipulation and separation of individual semiconducting and metallic nanowires”, *Nat. Photonics*, **2**, 86-89 (2008).

[8] Greenleaf W J, Woodside M T, and Block S M, “High-Resolution, Single-Molecule Measurements of Biomolecular Motion”, *Annu. Rev. Bioph. and Biom.*, **36**, 171-190 (2007).

[9] Wang M D, Yin H, Landick R, Gelles J, and Block S M, “Stretching DNA with optical tweezers”, *Biophys. J.*, **72**(3), 1335–1346 (1997).

[10] Jauffred L, Richardson A C, and Oddershede L B, “Three-Dimensional Optical Control of Individual Quantum Dots”, *Nano Letters*, **8** (10), 3376-3380 (2008).

[11] Zemanek P, Jonas A, Sramek L, and Liska M “Optical trapping of Rayleigh particles using a Gaussian standing wave**”,** *Opt Commun***, 151**, _273–285 (1998).

[12] Ashkin A, Dziedzic J M, Bjorkholm J E, and Chu S, "Observation of a single-beam gradient force optical trap for dielectric particles", *Opt. Lett*., **11**, 288-290 (1986).

[13] Righini M, Zelenina A S, Girard C, and Quidant R, “Parallel and selective trapping in a patterned plasmonic landscape*”, Nat. Phys.*, **3**, 477-480 (2007).

[14] Grigorenko A N, Roberts N W, Dickinson M R, and Zhang Y, “Nanometric optical tweezers based on nanostructured substrates”, *Nat. Photonics*, **2**, 365-370 (2008).

[15] Righini M, Volpe G, Girard C, Petrov D, and Quidant R, “Surface plasmon optical tweezers: tunable optical manipulation in the femtonewton range”, *Phys. Rev. Lett.*, **100**, 186804 (2008).

[16] Arnold S, Keng D, Shopova S I, Holler S, Zurawsky W, and Vollmer F, “Whispering gallery mode carousel – a photonic mehanism for enhanced nanoparticle detection in biosensing”, *Opt. Express*, **17**, 6230–6238 (2009).

[17] Barth M, and Benson O, “Manipulation of dielectric particles using photonic crystal cavities”, *Appl. Phys. Lett.*, **89**, 253114 (2006).

[18] Lin S, Hu J, Kimerling L, and Crozier K, "Design of nanoslotted photonic crystal waveguide cavities for single nanoparticle trapping and detection", *Opt. Lett.*, **34**, 3451– 3453 (2009).

[19] Mandal S, Serey X, and Erickson D, "Nanomanipulation Using Silicon Photonic Crystal Resonators", *Nano Lett.*, 10 99-104 (2010).

[20] Yang A H J, Moore S D, Schmidt B S, Klug M, Lipson M, Erickson D, "Optical Manipulation of Nanoparticles and Biomolecules in Sub-Wavelength Slot Waveguides", *Nature*, **457**, 71-75 (2009).

[21] Juan M L, Gordon R, Pang, Y, Eftekhari F, and Quidant R, "Self-induced back-action optical trapping of dielectric nanoparticles", *Nat. Phys.*, **5**, 915 - 919 (2009).

[22] Mandal S, Goddard J, and Erickson D, "A Multiplexed Optofluidic Biomolecular Sensor for Low Mass Detection" *Lab chip*, **9**, 2924-2932 (2009) .

[23] Velha P, Rodier J C, Lalanne P, and Hugonin J P, Peyrade D, Picard E, Charvolin T, and Hadji E, "Ultracompact silicon-on-insulator ridge-waveguide mirrors with high reflectance", *Appl. Phys. Lett.*, **89**, 171121 (2006).

[24] Jackson J D, "*Classical Electrodynamics*", Third Edition, John Wiley & Sons (1999).

[25] Svoboda K, and Block S M, "Biological Applications of Optical Forces", *Annu. Rev. Biophys. And Biom.*, **23**: 247-285 (1994).

[26] Gardiner C W, "*Handbook of Stochastic Methods: For Physics, Chemistry, and the Natural Sciences*", Third Edition, New York: Springer (2004).

[27] See for example chapter 3, de Fornel F, "*Evanescent waves: From Newtonian Optics to Atomic Optics*", Springer, 2000.

[28] Rohrbach A, " Stiffness of Optical Traps: Quantitative Agreement between Experiment and Electromagnetic Theory", PRL, **95**, 168102 (2005).

[29**]** Zemanek P, Jonas A, Jakl P, Jezek J, Sery M, and Liska M, **"**Theoretical comparison of optical traps created by standing wave and single beam", *Opt Commun*, 220, 401-412 (2003).

[30] Yang A H J, Lerdsuchatawanich T, and Erickson D, "Forces and Transport Velocities for a Particle in a Slotted Waveguide", *Nano Lett.*, **9**, 1182-1188 (2009).

[31] Zhu J, Ozdemir S K, Xiao Y-F, Li L, He L, Chen D-R, and Yang L, "On-chip single nanoparticle detection and sizing by mode splitting in an ultrahigh-Q microresonator", *Nat. Photonics*, **4**, 46-49 (2009).

CHAPTER 4

ANGULAR ORIENTATION OF NANORODS USING NANOPHOTONIC TWEEZERS

4.1 Abstract

Near-field optical techniques have enabled trapping, transport, and handling of nanoscopic materials much smaller than what can be manipulated with traditional optical tweezers. Here we extend the scope of what is possible by demonstrating angular orientation and rotational control of both biological and non-biological nanoscale rods using photonic crystal nanotweezers. In our experiments, single microtubules (diameter 25 nm, length 8 μm) and multi-walled carbon nanotubes (outer diameter 110 – 170 nm, length 5 μm) are rotated by the optical torque resulting from their interaction with the evanescent field emanating from these devices. An angular trap stiffness of κ = 92.8 pN·nm/rad^2-mW is demonstrated for the microtubules and a torsional spring constant of 22.8 pN nm/rad^2-mW is measured for the nanotubes. We expect that this new capability will facilitate the development of high precision nanoassembly schemes and biophysical studies of bending strains of biomolecules.

Reprinted with permission from *Kang,* Serey *et al.*, and the American Chemical Society, "Angular Orientation of Nanorods using Nanophotonic Tweezers" Nano Letters 12, 6400-6407 (2012).

4.2 Introduction

In 1987, Ashkin *et al*.[19, 20] showed that a single rod-shaped cell and bacteria and viruses could be trapped and oriented with laser beams, demonstrating optically induced rotation along with the optical trap[21]. In biophysical studies the orientation control of elongated objects is significant because numerous biomolecules such as DNA, viruses, and bacteria can take rod-like shapes[22]. Optical torque arises from the exchange of angular momentum between an electromagnetic field and a physical object. Circularly polarized laser beams carry angular momentum which can lead to a torque on dielectric objects[23-25]. Another general method is to take advantage of the interaction of anisotropic dielectric objects with light fields to provoke the change in angular momentum[26]. Padgett and Bowman[27, 28] recently reviewed the various methods for applying optical torques with conventional optical tweezers.

This capability is well established for traditional optical tweezers[27-30], but has not been addressed in the near-field trapping literature. Near-field optical traps are of particular interest because they allow for the trapping of smaller materials than conventional optical tweezers[31]. These devices take advantage of the increased gradient force exerted on particles due to a combination of highly confining light geometries and increased intensity due to resonances. Several different device structures has been exploited to this end including photonic crystal resonators[14, 32], ring resonators[33], and localized surface plasmons[34, 35] each providing very deep trapping potentials. Researchers have investigated ways of taking advantage of the

interaction of different polarizations of light with specially designed plasmonic structures to tune the position of trapped spherical particles around a plasmonic cylinder[35] or to continuously rotate a plasmonic object[36]. To date however the ability to simultaneously optically trap and reorient an unstructured nanoscale object has not been demonstrated. Orientation control is a particularly important issue to address for trapping of nanoscale objects since as the size of the trapped object decreases the rotational diffusion coefficient increases (analogous to linear diffusion). Adding orientation control to the capabilities listed above would allow for tight control over five out of six degrees of freedom.

In this paper, we characterize the optical torque arising in one dimensional photonic crystal resonators and demonstrate the orientation of rod-like biological (microtubules, MTs) and non-biological (carbon nanotubes, CNTs) materials. First, the dynamics of the orientation of MTs in the cavity of a photonic crystal resonator will be examined at different trapping laser powers and compared with an analytical model. In the second section we examine the capacity of the optical trap to maintain a rod's orientation and described it in terms of a torsion spring model. Experimental measurements of the torsion spring constant have been performed for the two materials of interest here (MTs and CNTs) to demonstrate the broad applicability of the technique. Finally, dynamic control over the orientation of carbon nanotubes via hydrodynamic flow is also demonstrated. In the below, experiments with biological samples are performed with a silicon nitride photonic crystal resonator operating at 1064 nm in a biological buffer (which was previously verified not to undergo significant temperature

increase[32]), whereas the experiments with carbon nanotubes were performed with silicon resonators in heavy water operating at 1550 nm. Multiwall carbon nanotubes of outer diameter 110-170 nm were used in this work. Details of the experimental procedures and device fabrication techniques are provided in the methods and materials section.

4.3 Torsion Spring Model and of Angular Trap Stiffness

The previous expression of the electromagnetic torque can be simplified for small angles where the torque can be seen to vary linearly with the angular displacement described by a torsional spring model on the nanorods[29]. This enables us to determine the strength of the torsional trap in direct analogue to the way spring stiffness models are used to characterize the stability of a positional trap. To verify the torsion spring model is valid for dielectric rods smaller than the electromagnetic hotspot, we first developed a FEM model of a nanorod-resonator system (COMSOL). In the model the probe object is a 2 μm long, 40 nm diameter, anisotropic rod (the axial permittivity was set to 12 and the transverse permittivity is that of water). The torque was calculated from the Maxwell stress tensor as a function of the orientation of the rod. The following quantity was integrated over a surface enclosing the rod:

$$\vec{T} = \oiint \vec{r} \times \overline{\overline{T}}_{Maxwell} \cdot \vec{n}\, dS \tag{4.3}$$

Where $\boldsymbol{r}$ is the position vector with respect to the center of the rod, $\bar{\bar{T}}_{Maxwell}$ is the Maxwell stress tensor, $\boldsymbol{n}$ is the outgoing normal to the integration surface. The result of the integration of the torque tensor was found to take a sinusoidal shape with

angular period π. The plot of this torque is presented in Figure 4.1(a). Around the stable trapping position ($\theta = 0$) the torque can be seen to vary linearly with respect to θ as one would expect considering the Taylor expansion of the sinusoidal fit. The plot of this torque is presented in Figure 4.1(a). Around the stable trapping position the torque can be seen to vary linearly with respect to θ.

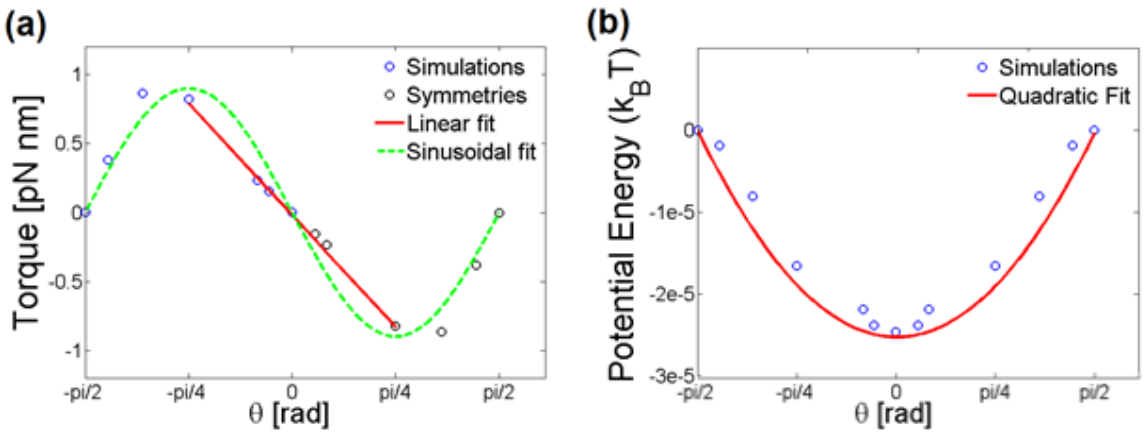

FIGURE 4.1. (a) Numerical computation of the torque exerted on an anisotropic rod by the means of Equation (4.1). The model rod is a 2 μm long, 40 nm diameter, anisotropic rod with longitudinal permittivity 12 and axial permittivity 1.72 same as the background water; it was placed 50 nm above a photonic crystal resonator on resonance[37] for angles in [-π/2,0]. Red dots represent the numerically estimated torques, blue dots represent the extrapolated ones with symmetries, and the green dotted line is a sinusoidal fit. The red line is a linear fit around θ=0 where the torque is linear in θ. (b) Rotational potential energy evaluated by integrating the torque with respect to θ. Red solid line is the quadratic potential to the linear fit in (a). Assuming a sinusoidal fit of the form sin(2θ) as displayed in (a), the quadratic potential should be valid for small angles where sin(2θ) is close to its first order Taylor expansion: 2θ.

A torsion spring representation of the torque in this region was therefore chosen to characterize the trapping properties of the photonic crystal resonators on the rods. Torsion springs are characterized by a constant κ called torsion spring constant. The torque and potential energy are given by:

$$\vec{T} = -\kappa\vec{\theta} \tag{4.4}$$

$$U_P = \frac{1}{2}\kappa\theta^2 \tag{4.5}$$

In these equations $\boldsymbol{T}$ is the torque and U_P is the potential energy. The potential energy was calculated from the torque and is presented in figure 4.1(b).

This way to describe the trapping capacity of photonic crystal resonator is useful as energy potentials allow for an easier comparison to other forces at play[38]. The torsion spring constant is linked to the angular spread measured experimentally through the equipartition theorem which, in the torsion spring model, reads:

$$\frac{1}{2}k_B T = \frac{1}{2}\kappa\left\langle\theta^2\right\rangle \tag{4.6}$$

In this equation k_B is the Boltzmann constant and T is the temperature in Kelvin. For microtubules, the torsional trapping stiffness was determined from Figure 4.2 (a) to be κ= 92.8 pN·nm/rad^2-mW (the torsion spring constant was normalized to the estimated power in the cavity). The average angular orientation θ_{mean} was measured from the center of the distribution was measured to 5.1° (0.088 rad) and the standard deviation was determined to σ = 3.1° (0.055 rad). Microtubules are representative of a dielectric material where the torque exerted by the photonic crystal should be well modeled by our spring constant analogy as illustrated by our numerical simulations. Because of the possible surface plasmon resonances in carbon nanotubes, they represent a special case of the theory. If the wavelength and k-vector coincide with a resonance of the CNT, the electric field will be further amplified as well as the torque. We account for this by making the trapping stiffness a function of θ: $\kappa(\theta)$. In the simplest

approximation, $\kappa(\theta)$ is a Lorentzian bell with a peak at $\theta = \theta_{mean}$. In this approximation the trapping stiffness at the steady position can be found through the equipartition theorem with $\kappa = \kappa(\theta_{mean})$. We present in Figure 4.2 (b) and (c) the comparison of the distribution of angles in the case of a trapped CNT and a freely rotating one (near the bottom of the microchannel). From Figure 4.2 (b) we compute the central stiffness to κ = 22.8 pN nm/rad^2-mW (normalized to the estimated power in the cavity). As can be seen from Figure 4.3 (b), the most likely position for the CNT was not orthogonal to the resonator, but at an angle of 35 degrees (0.61 rad). This is attributed to hydrodynamic forces, the shape of the CNT. Tong *et. al[39]* recently shown that plasmonic nanowires can orient orthogonally to the light polarization in optical tweezers if the beam waist is smaller than their length.

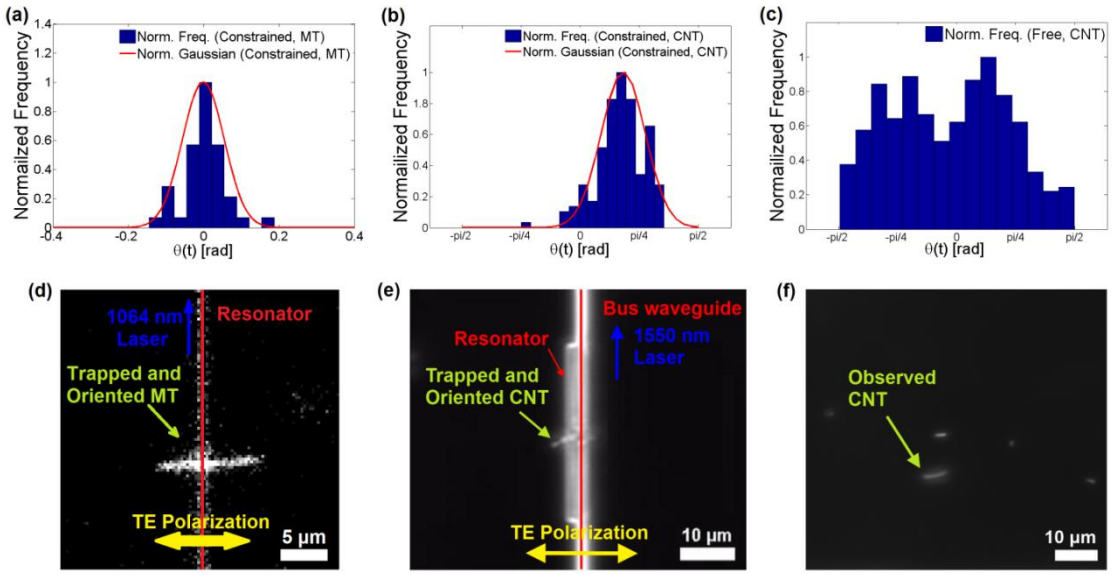

FIGURE 4.2. Analysis of the angular orientation of a trapped microtubule, carbon nanotube and a freely diffusing carbon nanotube. The angles were acquired every 0.1 second. (a) Histogram of orientations of a trapped microtubule. The red solid line represents a Gaussian fit. (b) Histogram of orientations of a trapped carbon nanotube. The red solid line represents a Gaussian fit. (c) Histogram of orientations of a freely diffusing carbon nanotube taken at the same focal plane as the resonator to account for viscous coupling with the Debye layer at the surface of the microchannel. (d-f) Sample frames from the data sets displayed in frames (a-c) respectively.

Because of the difficulty in numerically modeling CNTs, the experimental results of this work were not compared to theoretical predictions. The torsion stiffnesses in this study can be compared to that exerted by a far field optical tweezer. Porta and Wang[29] demonstrated an optical torsion spring as high as κ = 3360 pN·nm/rad on ~1 μm diameter quartz particles as compared to our 25 nm diameter microtubules.

The rotational motion was reduced when the nanorods were optically trapped and oriented, as shown in the previous paragraph. Additionally, the rate of diffusion was also found to be affected by the optical torsion spring. For a quantitative study of this observation, the rotational diffusion coefficient for MTs and CNTs in the presence and absence of the optical field were calculated from the measured angular displacements. The rotational diffusion coefficient relates to the angular displacement through the relation $D_\theta = \langle[\Delta\theta(t)]^2\rangle/(2t)$, where $\langle[\Delta\theta(t)]^2\rangle$ is time-averaged squared angular displacement[40]. The rotational Brownian motion of a freely rotating microtubule was observed at different heights in the flow channel. The rotational diffusion coefficient at the bottom of the channel ($D_{\theta,\text{free, MT}}' = 5.366\times10^{-2}$ rad^2/s) was lower than at mid channel height ($D_{\theta,\text{free, MT}} = 3.825\times10^{-1}$ rad^2/s) owing to viscous coupling[41] (Figure 4.3 (c) and (d)). The rotational diffusion coefficient is inversely proportional to viscosity as $D_r = k_B T/\pi\mu l^3 C r$, where C_r is a form factor $C_r = [3(\ln(l/r) - 1/2)]^{-1}$. The hydrodynamics coupling given rise from 7 times larger viscosity resulted lesser rotational diffusivity at the bottom of the channel. The apparent diffusion coefficient of an optically oriented microtubule, also at the bottom of the channel, was further

reduced to $D_{\theta,\text{cons, MT}} = 1.473\times10^{-2}$ rad^2/s, lower by a factor of 3.7 from $D_{\theta,\text{free, MT}}$ as seen in Figure 4.3 (a). Similarly, the diffusion coefficient of a carbon nanotube measured at the bottom surface ($D_{\theta,\text{free, CNT}} = 7.2\times10^{-2}$ rad^2/s) was observed to be higher by a factor of 4.1 than for a trapped CNT where we found $D_{\theta,\text{cons, CNT}} = 2.3\times10^{-2}$ rad^2/s (Figure 4.3 (b)).

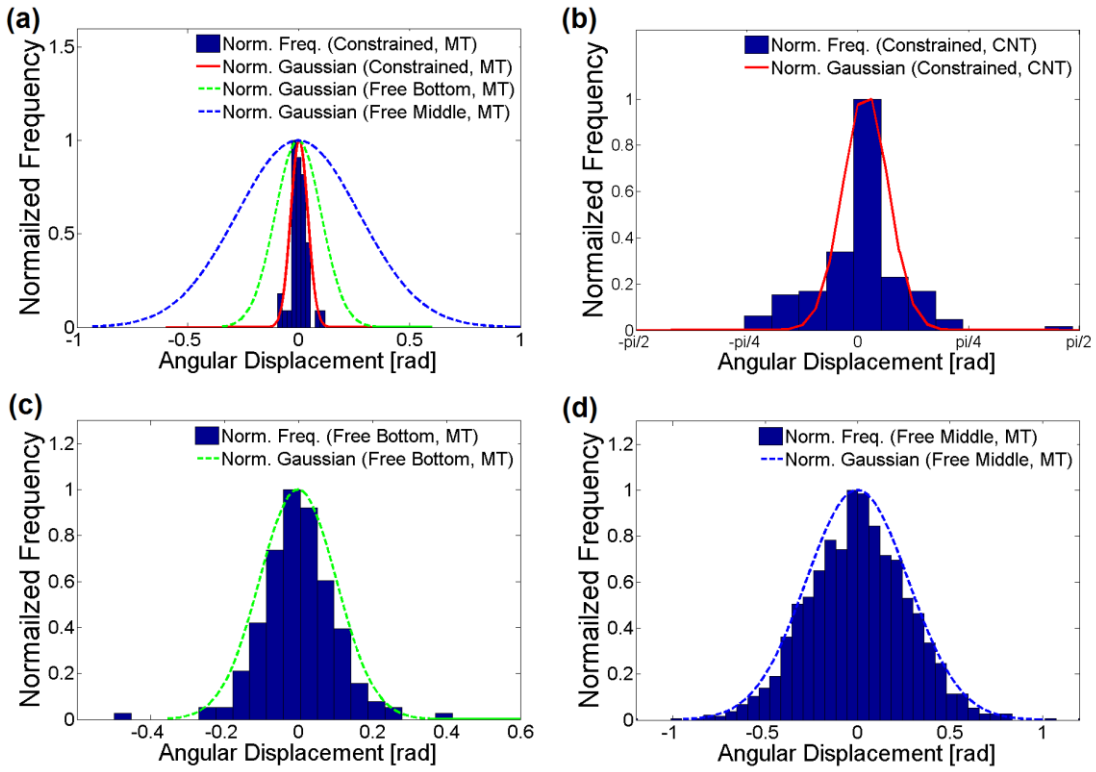

FIGURE 4.3. Histograms of angular displacement of trapped nanorods and of their free rotational Brownian motion. The orientation angle of the microtubule as a function of time $\theta(t)$ is measured every 0.1 second. The angular displacement as a function of time $\Delta\theta(t) = \theta(t+\tau_0) - \theta(\tau_0)$ is calculated for all angular trajectories with starting times, θ_0. (a) Comparison of the Probability Density Functions (PDF) of $\Delta\theta(t)$ for t = 0.1 s for a trapped microtubule and free ones. The normalized histogram (blue bars) and the normalized Gaussian fit (red solid line) of the constrained rotational Brownian motion are shown along with the normalized Gaussian fits of free rotational Brownian motion. (b) PDF of the angular displacement for t = 1 s of a trapped carbon nanotube. (c) PDF histogram (blue) and Gausian fit (green dotted line) of the angular displacement of a freely rotating microtubule at the same focal plane as the resonator to account for viscous coupling. (d) PDF histogram (blue) and Gausian fit (green

dotted line) of the angular displacement of a freely rotating microtubule at mid-channel height.

4.4 Hydrodynamic Torque

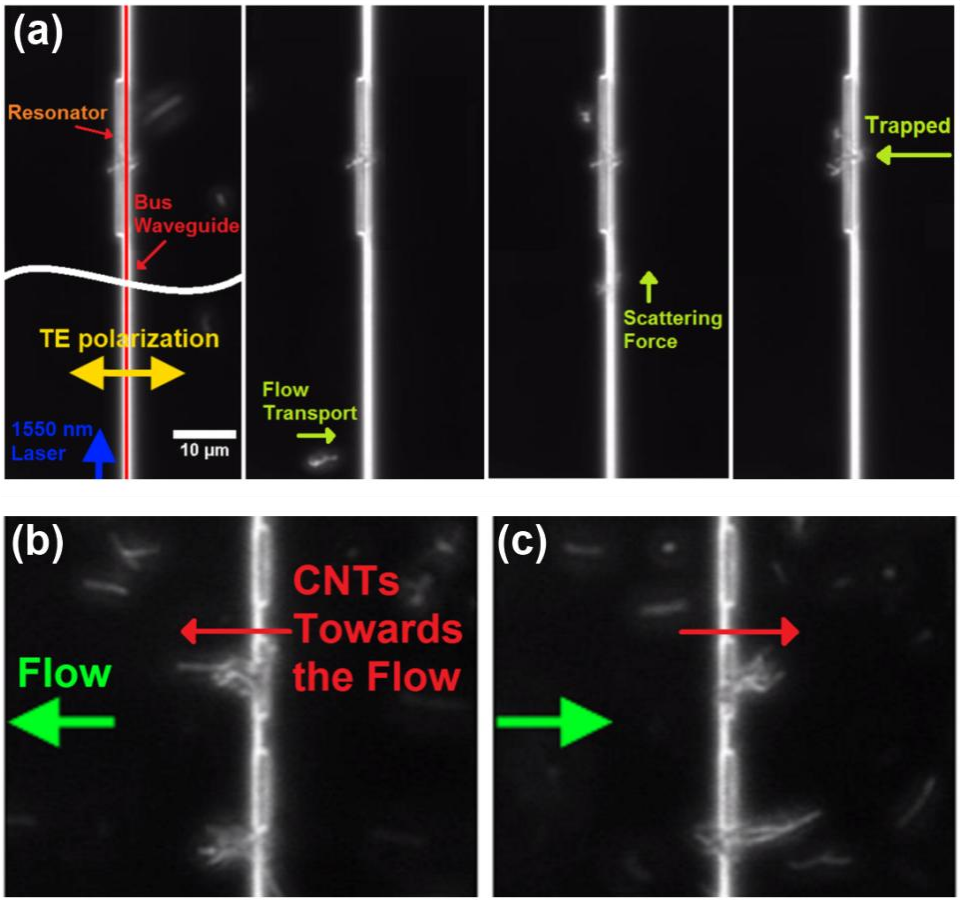

FIGURE 4.4. (a) Sequential image of trapping and orientation of a carbon nanotube observed under dark field microscopy. In the first image, a carbon nanotube is already trapped on the silicon PC resonator, another one is transported along the bus waveguide to the resonator where it remains trapped. Time lapse between the first and last frame is 10 s. For the sake of clarity, the images were retouched removing non-essential components. (b) and (c) Time lapse images of carbon nanotube aggregates. By switching the direction of the flow (green arrow), the hydrodynamic forces align the carbon nanotubes with the flow while the optical trap pins them to the resonator. (b) A flow rate of 30 µL/hour is applied with a mechanical syringe pump right to left. The carbon nanotubes point in the direction of the flow. (c) The flow direction is reversed, the nanotubes reorient to point in the direction of the flow. In this experiment, the flow channel was orthogonal to the bus waveguide.

The previous experiments were performed with little to no fluid flow in the microfluidic channel. Fluid flows, however, can balance the optical torque and offer another way to dynamically control the orientation of trapped nanorods. We describe here in qualitative terms the influence of the hydrodynamic torque on their orientation. In these experiments, hydrodynamic forces affect the CNTs initially as they are propelled upwards by the radiation pressure along the resonator as seen in Figure 4.4 (a). This radiation pressure transport along waveguides affect has been documented previously in our other works[14]. When moving along the resonator, the hydrodynamic forces tend to orient the nanotubes along their direction of motion until they come to the trap where they are quickly reoriented back to the orthogonal position. It is also observed that the resonator can only support two carbon nanotubes at a time. A third nanotube does not get trapped and is pushed upwards along the waveguide similarly to what was described by Cai *et al.*[42] in their tapered waveguide.

Hydrodynamic forces can also be used to actively orient the trapped carbon nanotubes. The carbon nanotubes were observed to be preferentially trapped close to their extremities. Taking advantage of the flow, which was orthogonal to the resonator, the carbon nanotubes were oriented left or right as shown in Figure 4.4 (b). The flow was applied with a mechanical syringe pump set at 30 μL/hour. At the surface of the substrate, the flow speed is lower because of the parabolic flow profile in a microchannel. The flow speed was estimated from the recorded video assuming the

smallest carbon nanotubes are good flow tracers. With this method the flow speed at the surface was measured to be 7.12 ± 1 μm/s. With more microfluidic ports, the orientation of the trapped nanotubes could have been chosen to cover nearly 2π spread with the microfluidic assembly line proposed by Schneider *et al.*[43].

4.5 Conclusion

Along with the ability to confine nanoscale material in solution, constraining their orientation ensures a level of control over five of six degrees of freedom that has not been demonstrated with other trapping techniques. Here, using photonic crystal resonators, the manipulation of microtubules and carbon nanotubes was demonstrated by studying the dynamics of the orientation in the dipole moment framework. The action of the electromagnetic field on nanorods was described as a torsion spring and the torsion spring constants were determined to 92.8 pN·nm/rad^2-mW for MTs and 22.8 pN nm/rad^2-mW for MWCNTs. Additionally, he rotational diffusion rate was observed to be reduced 4.7 times for a trapped MT compared to a freely diffusing one. We believe such tight grasp on biological and non-biological material should enable novel biophysical studies and find use in nanoscale assembly and material sciences.

4.6 Funding Sources

This work was supported by the U.S. Department of Energy office of basic science under grant DE-SC0003935.

4.7 Notes

D.E. declares an interest in a company (Optofluidics, Inc.) engaged in the commercialization of the commercialization of the NanoTweezer technology.

4.8 Acknowledgment

The authors would like to thank Matt Graham, of the Kavli Institute at Cornell, for useful discussions regarding single wall carbon nanotubes. This work was performed in part at the Cornell NanoScale Facility, and a portion of the calculations for this work were done on the Intel Cluster at the Cornell Nanoscale Facility, a member of the National Nanotechnology Infrastructure Network, which is supported by the National Science Foundation (Grant ECS-0335765). The authors appreciate access and the use of the facilities of the Nanobiotechnology Center (NBTC), an STC Program of the National Science Foundation under Agreement no. ECS-9876771.

REFERENCES

1. Ashkin, A., J.M. Dziedzic, and T. Yamane, *Optical Trapping and Manipulation of Single Cells Using Infrared-Laser Beams.* Nature, 1987. **330**(6150): p. 769-771.
2. Ashkin, A. and J.M. Dziedzic, *O Optical Trapping and Manipulation of Viruses and Bacteria.* Science, 1987. **235**(4795): p. 1517-1520.
3. Ashkin, A., *Acceleration and Trapping of Particles by Radiation Pressure.* Physical Review Letters, 1970. **24**(4): p. 156-159.
4. Miller, R.D. and T.B. Jones, *Electro-Orientation of Ellipsoidal Erythrocytes - Theory and Experiment.* Biophysical Journal, 1993. **64**(5): p. 1588-1595.
5. Allen, L., et al., *Orbital Angular-Momentum of Light and the Transformation of Laguerre-Gaussian Laser Modes.* Physical Review A, 1992. **45**(11): p. 8185-8189.
6. Friese, M.E.J., et al., *Optical angular-momentum transfer to trapped absorbing particles.* Physical Review A, 1996. **54**(2): p. 1593-1596.
7. He, H., et al., *Direct Observation of Transfer of Angular-Momentum to Absorptive Particles from a Laser-Beam with a Phase Singularity.* Physical Review Letters, 1995. **75**(5): p. 826-829.
8. Vogel, R., et al., *Synthesis and Surface Modification of Birefringent Vaterite Microspheres.* Langmuir, 2009. **25**(19): p. 11672-11679.
9. Padgett, M. and R. Bowman, *Tweezers with a twist.* Nature Photonics, 2011. **5**(6): p. 343-348.

10. Dholakia, K. and T. Cizmar, *Shaping the future of manipulation.* Nature Photonics, 2011. **5**(6): p. 335-342.

11. La Porta, A. and M.D. Wang, *Optical torque wrench: Angular trapping, rotation, and torque detection of quartz microparticles.* Physical Review Letters, 2004. **92**(19).

12. Schneider, C.A., W.S. Rasband, and K.W. Eliceiri, *NIH Image to ImageJ: 25 years of image analysis.* Nature Methods, 2012. **9**(7): p. 671-675.

13. Erickson, D., et al., *Nanomanipulation using near field photonics.* Lab on a Chip, 2011. **11**(6): p. 995-1009.

14. Mandal, S., X. Serey, and D. Erickson, *Nanomanipulation Using Silicon Photonic Crystal Resonators.* Nano Letters, 2010. **10**(1): p. 99-104.

15. Chen, Y.F., et al., *Controlled Photonic Manipulation of Proteins and Other Nanomaterials.* Nano Letters, 2012. **12**(3): p. 1633-1637.

16. Lin, S.Y., E. Schonbrun, and K. Crozier, *Optical Manipulation with Planar Silicon Microring Resonators.* Nano Letters, 2010. **10**(7): p. 2408-2411.

17. Juan, M.L., et al., *Self-induced back-action optical trapping of dielectric nanoparticles.* Nat Phys, 2009. **5**(12): p. 915-919.

18. Wang, K., et al., *Trapping and rotating nanoparticles using a plasmonic nano-tweezer with an integrated heat sink.* Nat Commun, 2011. **2**: p. 469.

19. Liu, M., et al., *Light-driven nanoscale plasmonic motors.* Nat Nano, 2010. **5**(8): p. 570-573.

20. Serey, X., S. Mandal, and D. Erickson, *Comparison of silicon photonic crystal resonator designs for optical trapping of nanomaterials.* Nanotechnology, 2010. **21**(30).

21. Serey, X., et al., *DNA Transport and Delivery in Thermal Gradients near Optofluidic Resonators.* Physical Review Letters, 2012. **108**(4).

22. Tong, L., V.D. Miljković, and M. Käll, *Alignment, Rotation, and Spinning of Single Plasmonic Nanoparticles and Nanowires Using Polarization Dependent Optical Forces.* Nano Letters, 2009. **10**(1): p. 268-273.

23. Han, Y., et al., *Brownian motion of an ellipsoid.* Science, 2006. **314**(5799): p. 626-630.

24. Minoura, I. and E. Muto, *Dielectric measurement of individual microtubules using the electroorientation method.* Biophysical Journal, 2006. **90**(10): p. 3739-3748.

25. Cai, H. and A.W. Poon, *Planar optical tweezers using tapered-waveguide junctions.* Optics Letters, 2012. **37**(14): p. 3000-3002.

26. Schneider, T.M., S. Mandre, and M.P. Brenner, *Algorithm for a Microfluidic Assembly Line.* Physical Review Letters, 2011. **106**(9): p. 094503.

CHAPTER 5

DNA DELIVERY AND TRANSPORT IN THERMAL GRADIENTS NEAR OPTOFLUIDIC RESONATORS

Nanoscale optofluidic resonators have recently proven themselves useful in fields ranging from chemical and biological sensing [1] to nano-manipulation [2, 3]. In most of these optofluidic devices, the transport of solutes to the electromagnetic hotspot is critical to the device's performance. The effects of hydrodynamic forces on trapping experiments have been characterized [4, 5], as well as the effect of plasmonic heat sources on the fluid flow [6]. In the past few years, the transport of molecules due to temperature gradients, often called thermophoresis [6, 7], has been shown to be an important phenomenon in molecular transport [8]. Recently, researchers have studied the effects of thermophoresis on plasmonic based sensing [9]. While the absorption of infrared (IR) light by water in the evanescent field of silicon photonic devices is expected to produce local heating, there is currently only a weak understanding of the magnitude of the effect and how it would affect the transport of molecules in the context of optical nano tweezing and silicon photonic biosensing.

Reprinted with permission from Serey *et al.*, and the American Physical Society, "DNA Delivery and Transport in Thermal gradients near optofluidic resonators" Physical Review Letters 108, 048102 (2012).

Here, we aim at demonstrating the effects of the optical absorption of water in the IR on temperature, flow dynamics, and λ-DNA transport in the vicinity of a silicon photonic crystal (PC) resonator. The temperature rise at the PC resonator leads to buoyancy forces that pinch the flow around the resonator while thermophoretic drift can either expel or attract particles from the resonator according to the signs of their thermophoretic coefficient. As in any thermophoretic event, the transport properties are strongly dependent on the species, medium, and temperatures considered [6]. In this paper, we first examine the heat generation and temperature field around the photonic cavity pointing out which parameters most significantly affect heat generation. We then study the flow around the cavity and the particle transport properties of λ-DNA. The 48 kbp λ-DNA is a molecule of particular interest due to its biophysical applications and whose thermophoretic properties have been characterized [6], additionally it has already been trapped by photonic devices [3]. Finally, we use thermodynamics and reaction rate theory to provide new understanding on how significantly common experiments, such as trapping, are likely to be affected by the heat production.

The photonic crystal (PC) resonators used in this study are standing wave resonators formed by the insertion of a periodic array of holes into a silicon waveguide. These holes surround a central cavity consisting of the bare silicon waveguide and, in some cases, an extremely small central hole as in Fig. 5.1(a). Discrete modes can exist in the cavity constituting a simple and effective optical trap [10] and sensor [11]. Because the electromagnetic field is enhanced, the improved interaction with the solution

results in a temperature increase which can be measured *in situ*. The devices were fabricated with standard e-beam fabrication procedures on a 250 nm silicon-on-insulator wafer. The experimental setup in this work consists of the silicon chip containing the photonic elements on top of which is assembled a transparent microfluidic channel. The ensemble is mounted on a microscope stage.

First numerical and experimental studies of the temperature increase near the photonic crystal resonator were performed. At the working wavelength of 1550 nm, water absorbs more than the optical materials present [12], so in our simulations all of the imaginary permittivities were ignored except for water ($\varepsilon'' = 3.51 \times 10^{-4}$ [13]). The electromagnetic to heat energy conversion was first computed numerically solving Maxwell's equations and used as a source term in the diffusive heat equation for a channel geometry of 500 micrometers wide, 125 micrometers high. Convective effects were numerically verified to be negligible as expected from the low Péclet number $Pe < 10^{-3}$. As seen in equation (5.1), the power lost to heat is proportional to the electromagnetic energy density and to the power input. The simulations are performed for 10 mW of power input, a commonly used power in experiments.

$$\kappa \nabla^2 T = \frac{\omega}{2} \times Im(\varepsilon) \times \left|\mathbf{E}\right|^2 (\vec{r}) \tag{5.1}$$

Here, T is the temperature, κ is the thermal conductivity of the material, ω is the resonant frequency, ε is the permittivity, and **E** is the electric field. In thin silicon beams, phonons-surface interactions cause the conductivity to change as compared to bulk silicon, this was taken into account by setting $\kappa = 100$ W m^{-1} K^{-1} [14]. It was found

that the maximum temperature increases is 57 K for cavities with a central hole as plotted in Fig. 5.1(b).

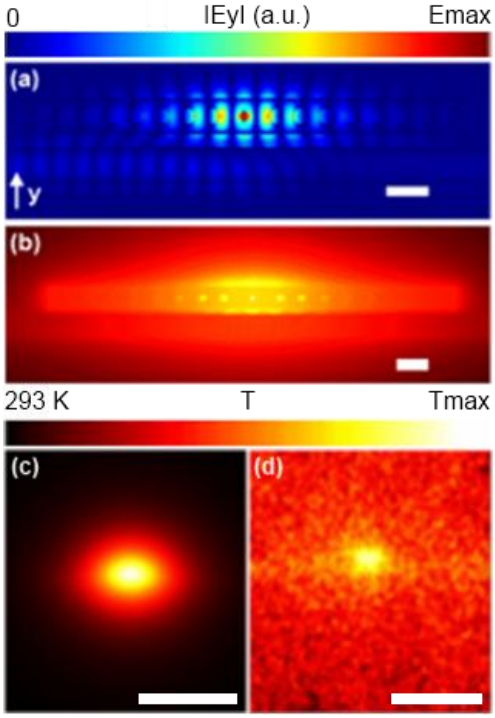

FIGURE.5.1. Scale bars: 500 nm (a,b), 15 μm (c,d). (a) Modulus of Ey in a PC resonator with a central hole. The light is coupled from the bottom waveguide. (b) Numerical estimation of the temperature increase of a PC resonator with a central hole. The maximum temperature is 350 K. (c) Numerical estimation of the temperature 2 μm above the resonator. For 1.7 mW of power input. The maximum temperature reached is 4 K. (d) Fluorescently measured temperature increase for 1.7 mW of estimated power input, 2 μm above the surface of the resonator. The maximum temperature increase is 4.8 K after correction for bleaching and thermophoresis of the rhodamine B.

In the central hole, the superposition of evanescent fields allows for a high field enhancement [3]. The field intensity's full strength interacts with the water leading to a particularly high temperature increase there. Experimentally, temperature sensitive fluorescent dye Rhodamine B was used to measure the temperature 2 micrometers

above the resonator. Correcting for the imaging defects, Fig. 5.1(d) was obtained. The maximum temperature increase measured of 4.8 $\mp$ 1 K. The measurement was carried out at an estimated power input into the resonator of 1.7 $\mp$ 0.3 mW. The numerical code took bleaching into account whereas the correction for thermophoresis was inferred from the experimental results published by Cordero *et al.*[15]. The measured temperature increase is 20% higher than the predicted 4 K increase for 1.7 mW of power input (Fig. 5.1(c)). The agreement offered validation of the theoretical calculation. Details of these experiments are provided in Chapter 5.

Following the thermal characterization, the transport properties of species near the PC resonator were examined. Numerical simulations were carried out to solve the steady state incompressible Navier-Stokes equation in the microfluidic environment (Equation 5.2). The effect of the thermal non-equilibrium was accounted for using the Boussinesq approximation (Equation 5.3). The validity of the Boussinesq approximation here is justified by the extremely low Grashof and Rayleigh numbers in 10 micrometers high microfluidic channels [16]. The Grashof number is defined as $Gr = g\beta(T_m - T_0)D_h^3/\nu^2 < 10^{-3}$ and the Rayleigh number is $Ra = g\beta(T_m - T_0)D_h^3/\nu\alpha < 10^{-3}$ (SI). Here, g is the standard gravity, β, ν, and α, are the thermal expansion coefficient, kinematic viscosity, and thermal diffusivity of water respectively. T_m and T_0 are the maximum and ambient temperature, and D_h is the hydraulic radius.

$$\rho \mathbf{u} \cdot \nabla \mathbf{u} = -\nabla \mathrm{p} + \mu \nabla^2 \mathbf{u} + \mathbf{f} \tag{5.2}$$

$$\mathbf{f} = -\mathbf{g}\left(\rho(T) - \rho(T_0)\right) \tag{5.3}$$

In these equations, ***u*** is the flow speed, p the pressure, ρ and μ are the density and viscosity of water, ***g*** is the standard gravity, and ***f*** is the Boussinesq buoyancy term. The result of these simulations is detailed in the SI. λ-DNA is often used as flow tracer because it follows the streamlines at steady state. However, in the presence of temperature gradients, their velocity needs to be corrected for thermal drift [6]. Thermophoresis is the movement of particles induced by temperature gradients, as expressed in equation (5.4). After correcting the flow streamlines for thermophoresis, we obtain actual pathlines followed by DNA molecules. As can be seen, the pathlines avoid the resonator and the region behind it is depleted (Fig. 5.2 and SI). Also importantly, the pathlines feature stop-points behind the resonator where the λ-DNA is trapped due to the opposition of the thermal drift and the fluid flow. This effect was demonstrated as a molecule trap by Duhr *et al*. [17]. The peculiar accumulation and depletion are best expressed in terms of concentration profile. The steady state concentration profile was computed as the solution of the convection-diffusion equations (5.5) corrected for thermophoretic flow:

$$\mathbf{u_T} = -D_T \nabla T, \tag{5.4}$$

$$\nabla \cdot \left(c\left(\mathbf{u} + \mathbf{u_T}\right) - D\nabla c\right) = 0. \tag{5.5}$$

Here, c is the concentration, **u** the velocity profile imported from the Navier-Stokes solution, $\mathbf{u_T}$ is the thermophoretic flow, and D and D_T are the diffusion coefficients

and the thermophoretic coefficient (0.8 $\mu m^2 s^{-1}$ and 0.9 $\mu m^2 s^{-1} K^{-1}$ respectively measured for 48 kbp λ-DNA in 1 mM Tris at 20°C by Duhr *et al.* [6]).

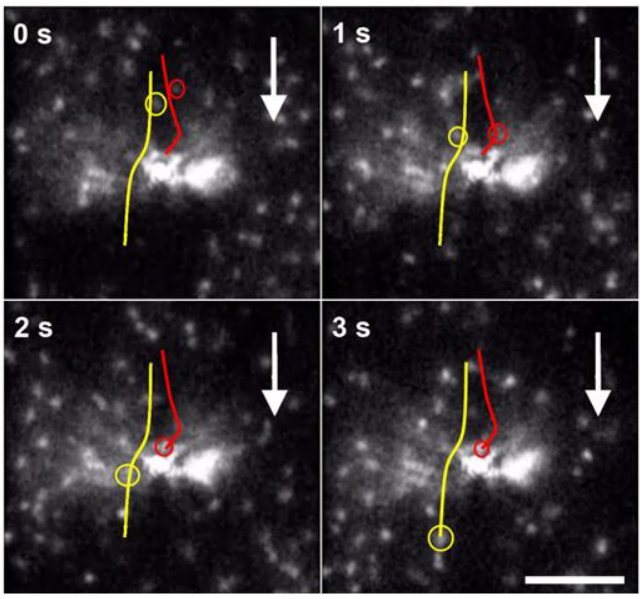

FIGURE 5.2. Times steps showing λ-DNA transport near the optical resonator (bright central light). White arrow represents the direction of the flow. Flow rate is 12500 $\mu m^3/s$. One molecule contours the photonic crystal (yellow online), while one is thermally trapped. Scale: 50 μm.

Experimentally, the concentration profile was measured from flowing λ-DNA (Fig. 5.2) in 1 mM Tris, 1 mM NaCl, buffer at 12500 $\mu m^3/s$ around a 1D photonic crystal resonator that was excited at the resonant frequency. The time-integrated intensity at each pixel was related to the concentration profiles under an ergodic assumption. A comparison of the experimental concentration profile with the numerical result is presented in Fig. 5.3. The concentration profile is shown to be consistent with simulations. In particular, as predicted from the simulation, the concentration profile exhibits an accumulation region in front of the resonator. Both numerically and experimentally, we observe a 3-fold increase ($c_{exp}/c_0 = 3.2 \mp 0.28$, $c_{num}/c_0 = 2.9$) of the

concentration at the thermal trap. A depletion region behind the resonator is also visible experimentally and numerically (c_{exp}/c_0 = 0.87 ∓ 0.05, c_{num}/c_0 = 0.7, 25 micrometers behind the resonator). Differences between the calculated profile and the experimental profile are accounted for by the experimental method (background fluorescence from molecules out of focus, averaging in the Z direction over the depth of field, and variations in flow speed and coupled power) and by the numerical assumption that the thermophoretic coefficient is temperature independent [18]. As the thermophoretic coefficients tend to increase with temperature, a higher than calculated accumulation was to be expected. It is important to note that although there is an accumulation in advance of the resonator, this effect significantly reduces species transport to the electromagnetic hotspot. It would therefore negatively impact biomolecular sensing and optical trapping.

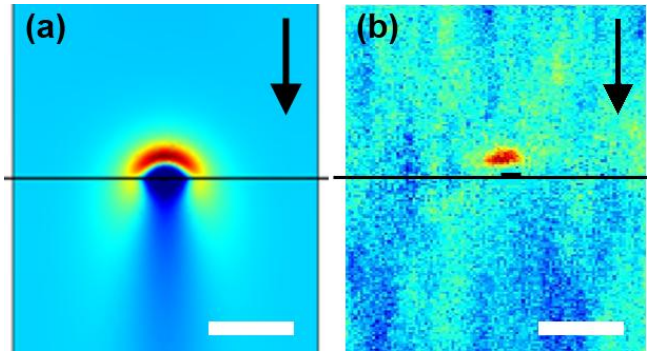

FIGURE 5.3. (a) Numerical (b) and experimental concentration profile in the vicinity of a PC resonator with a central hole. Power input is 10 ± 1 mW, and the flow is oriented top down at 12500 $\mu m^3/s$. The red spot corresponds to the thermophoretic trap due to opposed thermal and convective flows. Black lines: feeding waveguides. Black arrow represents the direction of the flow. Scale bars: 25 μm.

In the presence of thermal effects and drag forces, the free energy is evaluated by the means of equation (5.6) wherever the local equilibrium condition $\nabla T \le \left(a \times D_T / D\right)^{-1}$ is met [6], with a the hydrodynamic radius (SI).

$$c(\mathbf{r}) = c_0 e^{-F(\mathbf{r})/k_B T} \tag{5.6}$$

In this equation c is the steady state concentration, c_0 is the bulk concentration, $F(\mathbf{r})$ and $k_B T$ are the total free energy and the thermal energy fluctuation at the position $\mathbf{r}$ respectively. As seen in the concentration profile, this thermo-chemical free energy leads to a minimum where molecules accumulate (Fig 5.4b). At the resonator, the free energy is the highest for molecules with positive thermophoretic coefficient, such as λ-DNA, which are therefore repelled. To this free energy, we must add the electromagnetic potential created by the photonic trap. The electromagnetic hotspot is the global minimum of the potential energy and therefore a stable position for molecules. The thermo-chemical free energy barrier is as high as 12 $k_B T$ for 10mW of power input and spans a few micrometers range whereas the electromagnetic potential well is very deep in comparison (thousands of $k_B T$) but spanning a range of few hundred nanometers. The resulting superposition is sketched in Fig. 5.4(a,b). The absolute minimum of the potential energy, the electromagnetic well, is surrounded by a free energy barrier. The metastable minimum, which is the thermal accumulation point, is accessible to the molecules of the solution as it is not surrounded by a potential barrier. Last, entropic free energies should be added when confining macromolecules in small spaces [19], but have been ignored here when compared to

the electromagnetic potential. Flow drag tends to pull particles out of the trap but is also negligible for traps of hundreds of k_BT [5].

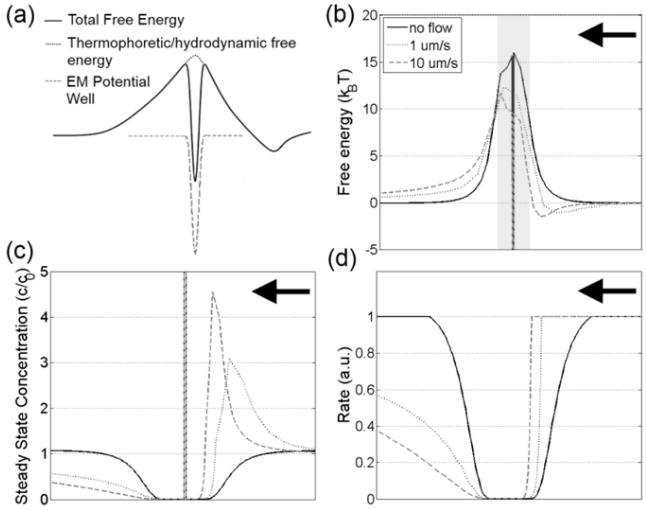

FIGURE 5.4. (a) Sketch of the superposition of the free energy resulting from the thermodiffusion and the electromagnetic well. (b-d) Numerical estimations along the flow direction (Y direction, horizontal scale: -50 μm to 50 μm, volumetric flow rate 12500 $\mu m^3/s$) for 10mW of power input. The legend in (b) applies to (c-d) as well. (b) Free energy diagram in k_BT units. At the resonator, the electromagnetic potential well is added to the free energy. The EM potential well is much deeper than the free energy barrier but spans a smaller region. The potential barrier is about 12 k_BT. The arrow represents the flow direction. Grey area represents the region where the local equilibrium criteria is not met, hence the free energy expansion (equation 5.6) is less accurate (SI). (c) Concentration profile. Even with no superimposed flow, we notice a small accumulation in the vicinity of the resonator. This is the result of the buoyancy induced convective flow (SI and [20]). (d) Diffusion rate estimated from the energy barrier through (5.7). At the resonator, the rate is 1/300000 times the average diffusion time.

In the steady state, the concentration profile is related to the energy profile by the Boltzmann distribution (5.6), where the two metastable states are populated (Fig. 5.4c). The depth of the electromagnetic well is weakly affected by the free energy, therefore the trapping remains very stable and steady state population of the optical trap should remain high. In the presence of the thermal field, the optical trap is now

surrounded by an energy barrier. The reaction rate theory provides valuable information about the dynamical picture. Reaction rates theory relates the energy barrier in the context of reaction kinetics [21] to the reaction rate as first explained by Kramers and seen in equation (5.7).

$$k(\mathbf{r}) = 2\pi k_0 e^{-\Delta F(\mathbf{r}) / k_B T} \tag{5.7}$$

Here, k is the trap/escape rate, k_0 is the reference trap/escape rate, and ΔF is the energy barrier. The 2π factor comes from the integration over the upper half sphere. For a molecule to be trapped optically, it first needs to tunnel through the energy barrier, leading to a very low trap rate (Fig. 5.4d). In trapping experiments, for molecules with high thermophoretic coefficient, the average trapping time is evaluated as the inverse of the trapping rate. From 5(d), the average time for a molecule to diffuse into the optical trap is 300,000 times longer than to be thermally trapped. The energy barrier's height was numerically found to be proportional to the factor $S_T P_{in}$. The Soret coefficient S_T is defined as the ratio of D_T/D. The term P_{in} is the laser power input. By linearity of the wave and heat equations, the temperature increase is proportional to the power input as long as heat conduction dominates convection. Under this condition and as long as the Soret coefficient can be considered to be independent of temperature, the former result holds. This result is intuitive from an energy standpoint when the local equilibrium condition is met.

In conclusion, we have studied the effect of heat generation on the transport of solutes to an optical resonator. Thermophoresis was found to play an important role in particle

transport near the resonator significantly reducing the local concentration at the electromagnetic hot-spot, thereby negatively affecting the performance of these devices as biomolecular sensors. These effects were further explained in thermodynamic terms using the formalism of reaction kinetics. These results should pave the way for new designs of optofluidic nanotweezers and biosensors that will avoid thermal effects or take advantage of them.

Elements of this work were funded by the US NSF (#0708599), US Department of Energy (DE-SC0003935), and US NIH (1R21EB009202). YFC was partially supported by a post-doctoral fellowship from the Kavli Institute at Cornell for Nanoscale Sciences.

REFERENCE

[1] H. K. Hunt and A. M. Armani, Nanoscale **2**, 1544 (2010).

[2] D. Erickson, *et al.*, Lab on a chip **11**, 995 (2011).

[3] A. H. J. Yang, *et al.*, Nature **457**, 71 (2009).

[4] K. Khosla, *et al.*, Arxiv, arXiv:1011.3897v1 (2010).

[5] A. H. J. Yang and D. Erickson, Nanotechnology **19**, (2008).

[6] J. S. Donner, *et al.*, ACS Nano null (2011).

[7] S. Duhr and D. Braun, Proc. Natl. Acad. Sci. U. S. A. **103**, 19678 (2006).

[8] A. Wurger, Rep. Prog. Phys. **73**, (2010).

[9] T. Kang, *et al.*, Small **6**, 2649 (2010).

[10] X. Serey, S. Mandal and D. Erickson, Nanotechnology **21**, (2010).

[11] S. Mandal and D. Erickson, Optics Express **16**, 1623 (2008).

[12] T. Asano, B. S. Song and S. Noda, Optics Express **14**, 1996 (2006).

[13] G. M. Hale and M. R. Querry, Appl. Opt. **12**, 555 (1973).

[14] K. E. Goodson and Y. S. Ju, Annual Review of Materials Science **29**, 261 (1999).

[15] M. L. Cordero, *et al.*, Phys. Rev. E **79**, (2009).

[16] D. D. Gray and A. Giorgini, Int. J. Heat Mass Transf. **19**, 545 (1976).

[17] S. Duhr and D. Braun, Phys. Rev. Lett. **97**, (2006).

[18] J. Han and H. G. Craighead, Science **288**, 1026 (2000).

[19] J. S. Donner, *et al.*, ACS Nano **5**, 5457 (2011).

[20] H. Grabert, Phys. Rev. Lett. **61**, 1683 (1988).

CHAPTER 6

EXPERIMENTAL ESTIMATION OF TEMPERATURE AND DNA TRANSPORT

This chapter is contains the supplementary information submitted with "DNA DELIVERY AND TRANSPORT IN THERMAL GRADIENTS NEAR OPTOFLUIDIC RESONATORS" as well as other methods unpublished.

6.1 Experimental setup

The experimental setup consists of a tunable fiber laser (tuning range: 1520 – 1620 nm) which signal is amplified through an EDFA and polarized through a paddle polarizer. The fiber output is a tapered fiber coupled to the chip with an inversed nanotaper [44]. The tapered fiber is mounted on a translation stage to facilitate coupling. The light out of the chip is coupled through a lense to a power meter. The microfluidic chip consists of a PDMS channel plasma bonded to the photonic chip so that the orientation of the waveguides is orthogonal to the flow. The fluid-flow is controlled with a syringe pump. The opto-fluidic chip is placed on a translation/rotation stage below an upright epifluorescent microscope.

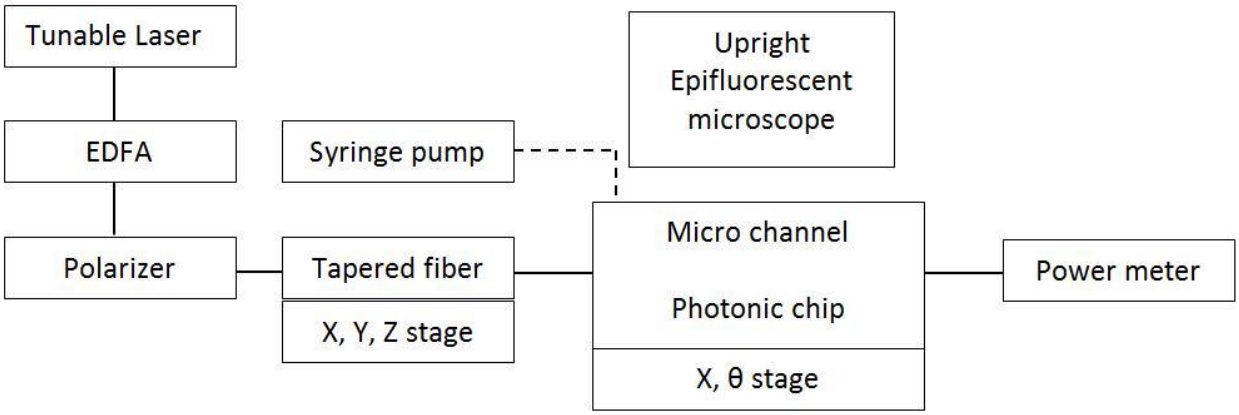

FIGURE 6.1. Schematic view of the experimental setup. The solid lines represent the laser light path outside the path. Dashed lines represent the flow path outside the chip.

6.2 Measurement of the temperature

Experimentally, temperature sensitive fluorescent dye Rhodamine B was used to measure the temperature 2 microns above the resonator. The quantum yield of rhodamine B is temperature dependent and has been well characterized[45]. A 50μM solution of Rhodamine B in carbonate buffer (pH 9.6) allows a good characterization of temperature changes at room temperature. This method is very effective for measuring temperature changes in situ, although the resolution is limited by the imaging technique (spatial resolution), by the bleaching (temperature resolution), and by the thermophoresis of the rhodamine dye, which effects were accounted for[45]. Because of the finite depth of field of our setup (1.3 μm to 3 μm depending on the objective used), the measured light intensity is the result of an averaging over different heights in the channel. We compare the measured temperature to the vertical average

of its numerical estimation. Furthermore, the solid parts of the chip do not contribute to the fluorescent measurement so we performed the measurement 2 micrometers above the resonator. The good agreement between experimental data and the corrected numerical estimation validates our modeling. We infer that the maximal temperature increase under 10mW of power input is as high as 50K.

6.3 Temperature distribution for resonators with or without a central hole

Two types of resonators were characterized in this study. Both consist of evanescently coupled 1D photonic crystal resonators, periodic arrays of circular holes in a 450 nm wide silicon beam. The periodicity (390 nm) and the hole radius (100 nm) is the same for both. The difference lies in the cavity. For one of them, the cavity consists of a 590 nm separation between two holes. For the other one, the cavity consists of 980 nm separation between two holes and the addition of a 50 nm radius hole at the center. In the central hole, the superposition of the evanescent fields results in a very high field intensity in the water. In the cavity without the central hole, the field is the highest in the silicon bulk. At the resonator, the temperature profiles are different because of the difference on volumetric heat production.

Further away from the resonators (1 micrometer above), the distribution of the temperature is averaged by the diffusion process and the profiles of the two types of resonators are no longer differentiable.

6.4 Analytical estimation of the heat produced by the optofluidic resonator

The total heat produced H can be expressed as

$$H = \frac{\omega}{2} \times \int \mathrm{Im}(\varepsilon) E^2 dV \tag{6.1}$$

With ω the light frequency, ε the permittivity, and E the electric field. We can rewrite H in simpler terms assuming only water absorbs the electromagnetic energy:

$$H = \frac{\omega}{2} \frac{\mathrm{Im}(\varepsilon_{water})}{\mathrm{Re}(\varepsilon_{water})} f V_{eff} \max(\mathrm{Re}(\varepsilon E^2)) \tag{6.2}$$

Where V_{eff} is the field volume, and where we introduced the fraction of the field in water

$$H = \frac{\omega}{2} \frac{\mathrm{Re}(\varepsilon_{water}) \int_{water} E^2 \, dV}{\int_{everywhere} \mathrm{Re}(\varepsilon) E^2 \, dV}$$

Approximating the circulating intensity to be proportional to *Q/V* (it is not an approximation is the case of circulating wave resonators), we finally show the proportionality:

$$H \propto \omega \frac{\mathrm{Im}(\varepsilon_{water})}{\mathrm{Re}(\varepsilon_{water})} f \times Q \tag{6.3}$$

In these equations V_{eff} is the mode volume and *Q* is the quality factor of the cavity.

This relation points out the most important factors contributing to heat production and quantifies their impacts. Developing new optical traps, one desires to minimize the heat produced while keeping the optical force high. The increase of the trapping force is often related to an increase of the field intensity and a better confinement (Q/V). One should therefore change *f* or the absorption coefficient in order to reduce losses to

heat. Reducing *f* is difficult in practice because of the evanescent field. In the case of the resonator, the contribution to the heat of the central hole was 10% of the total heat. Although the field is higher in the central hole, it spans a very small region. The most efficient way to decrease the heat produced is to reduce the absorption coefficient, which can be achieved either by changing the medium (for example heavy water has a similar refractive index but its absorption coefficient is only ε''=1.25e-5 [46]) or the wavelength (water has a transparency window in the visible light).

6.5 Flow and transport.

The flow dynamics of the microfluidic channel in the presence of buoyancy forces were numerically calculated. The simulations consisted of Finite Element Method numerical solutions to the stationary imcompressible Navier-Stokes equations. The Boussinesq approximation was used to include buoyancy.

$$\rho\left(\vec{u}\cdot\nabla\right)\vec{u} = -\vec{\nabla}p + \mu\nabla^2\vec{u} + \vec{f} \tag{6.4}$$

$$\vec{f} = -\vec{g}(\rho(T) - \rho(T_0)) \tag{6.5}$$

In these equations, $\boldsymbol{u}$ is the flow speed, p the pressure, ρ and μ are the density and viscosity of water, $\boldsymbol{g}$ is the standard gravity, and $\boldsymbol{f}$ is the Boussinescq buoyancy term. Although the temperature increase is as high as 50K (17% increase of the bulk temperature). The applicability of the Boussinesq approximation is provided by the low Grashoff and Rayleigh numbers calculated for a 20 micrometers high channel.

$$Gr = \frac{g\beta\left(T_m - T_0\right)D^3}{\nu^2} = 2.7\times10^{-4} \text{ and } Ra = \frac{g\beta\left(T_m - T_0\right)D^3}{\nu\alpha} = 2\times10^{-3}.$$

Where β is the thermal expansion coefficient, T_m and T_0 are the maximum and bulk

temperatures, D is the hydraulic diameter, ν is the kinematic viscosity, and α is the thermal diffusivity. Because the fluidic system is a microfluidic device, they are both found to be extremely low ($Gr<10^{-3}$ and $Ra\sim10^{-3}$), in which regime the approximation is justified [47].

From these simulations we extract the flow streamlines for several flow speeds. We find that eddies, with currents up to 100s of nanometers per second as seen in Fig. 6.2a, can occur due to the temperature increase in the absence of flow, agreeing with recently published results [48]. The usual flow speeds used experimentally (on the order of 1 μm/s) are too high to allow for the apparition of eddies. Instead, the flow lines near the resonator seem to be pinched around it (see Fig 6.2b). This is the result of the superposition of eddies with the Poiseuille flow profile. Physically, the water at the warm spot is pushed upwards by the buoyancy forces because its density is lower at higher temperatures. The depletion in water leads to an effective "negative pressure" that attracts the incoming streamlines. In the absence of other effects, solutes should therefore be more likely to hover above the optical trap than without thermal effects.

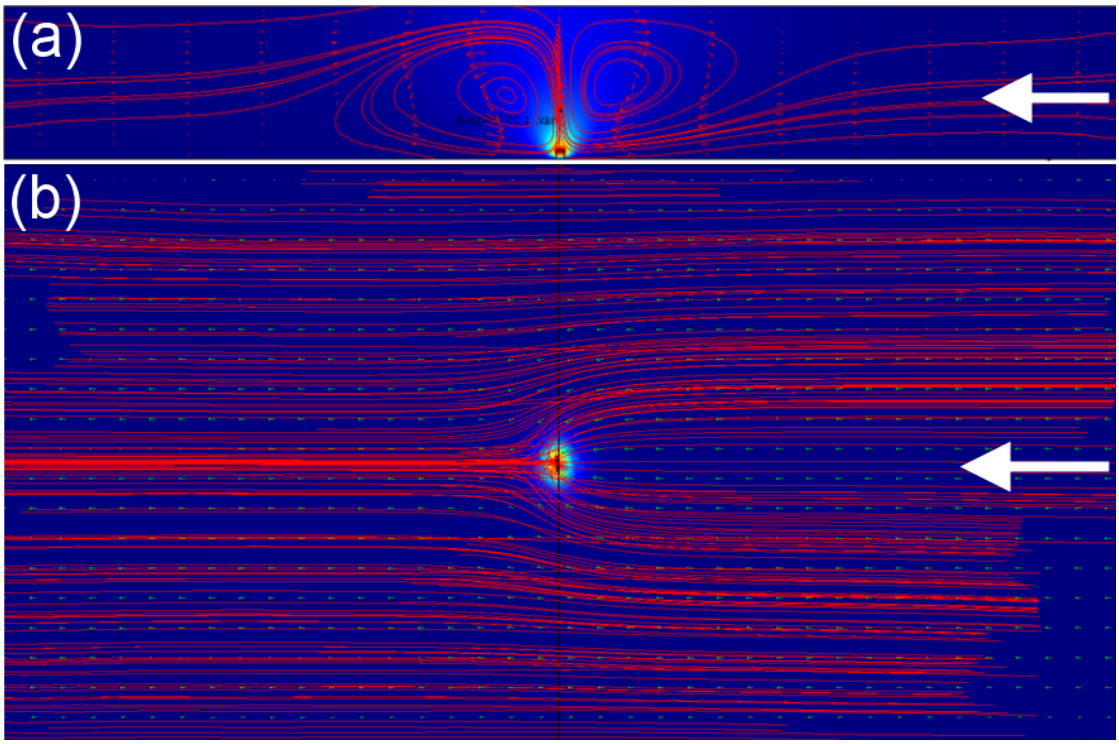

FIGURE 6.2. Buoyancy forces on the microfluidic flow. (a) Numerical solution (2D) for a 80K temperature increase and 0.1 μm/s flow. (b) Numerical solution (3D) for a resonator in a microchannel geometry with a 57K temperature increase and 1 μm/s flow. The flow lines are pinched around the resonator. Arrow represents the flow direction.

The solutes do not follow the flow lines but seem to avoid the resonator. The explanation lies in the thermal migration of the λ-DNA molecules. Solutes follow the pathlines dictated by thermophoresis. These were calculated from the numerical solution to the Navier-Stokes equation by computing the streamlines corrected for thermophoresis $\mathbf{u} + \mathbf{u}_T$, as seen in FIG 3.

The case of λ-DNA is of particular interest not only because of its possible applications experimentally, but also because the thermal migration of λ-DNA has been well characterized [49].

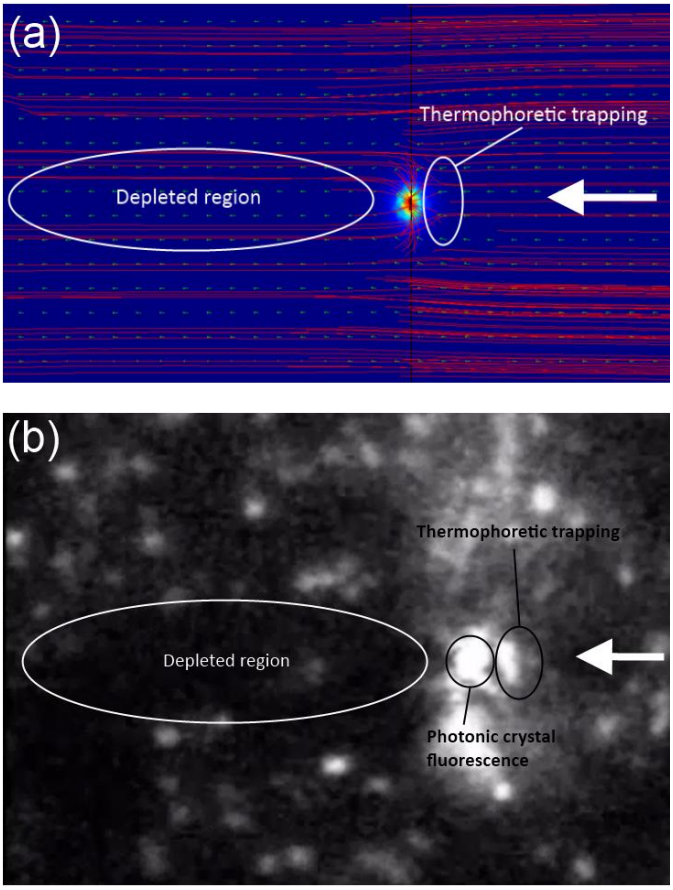

FIGURE 6.3. Correction for thermophoresis. (a) Numerical solution (3D) for a resonator in a microchannel geometry with a 57K temperature increase and 1 μm/s flow, corrected for thermophoresis. The path lines are no longer pinched around the resonator but instead we observe thermophoretic trapping and a depleted region behind the resonator. (b) instant shot from attached video showing the trapping and the depleted region. Arrow represents the flow direction.

6.6 Free energy expansion

It is an ongoing debate in the thermophoresis field when and how much a local equilibrium picture describes the thermophoretic events. This work is not intended to resolve this discussion and the free energy is calculated as a mean to compare thermophoretic effects on other physical phenomena (the electromagnetic potential, drag forces, and entropic forces). This point of view is the only one allowing for a quantitative comparison although it is not universally valid. Additionally, time

dependant parameters are extracted from this steady state picture thanks to the use of Kramers' relation. To the best of our knowledge, this has not been done previously.

Duhr *et. al* derive the condition $\nabla T \leq \left(a \times S_T\right)^{-1}$ to mark the domain of validity of the local equilibrium approximation [50]. It is therefore clear that depending on the optical system, on the amount of heat produced, and on the molecules/species involved, the approximation can hold or not. In our experiment, for 48 kbp λ-DNA the approximation only holds for molecules 4 micrometers away from the resonator. The calculation of the free energy is therefore less accurate in the near vicinity of the resonator.

For the sake of consistency the numerical results in Fig. 4 were performed for the same system as in the experiment presented albeit not in local equilibrium everywhere. The conclusions from these calculations are easily applied to slight variations of the system: An optical trap with a power input of 1 mW should be able to trap the λ-DNA molecules while being in local equilibrium everywhere.

6.7 Concentration measurement

In single or few molecules experiments, measuring concentrations is challenging because there aren't enough molecules for the usual continuous assumptions to hold. It is to say that it is not possible to measure that there are twice as many molecules in one spot as compared to another because there might only be one molecule in the field of view. It is possible however to keep track of the few molecules in the field of view and count where they spend the most of their time. We therefore get a map of how much time each molecule spent at each spot. We can directly count the amount of time

spent by molecules at each spot with fluorescent microscopy. Under an ergodic assumption, averaging the amount of time spent by molecules at each spot will be proportional to the concentration.

In a fluorescence experiment, we record the fluorescent signal from molecules in the field of view over time. In post processing, we can integrate the intensity of the light hitting each pixel over the duration of the video. At any time, the intensity of each pixel is proportional to the number of fluorophores at that position. The result of the integration provides us with a quantity proportional to the integral of the concentration over time.

More precisely after averaging, we expect to obtain at each pixel an estimation of the quantity:

$$C_{pixel} = \frac{1}{T}\int_0^T c(t)dt \tag{6.6}$$

In one dimension we can input the usual time dependence of the concentration and see that this expression converges to the steady state concentration as T increases:

$$C_{pixel} \sim \frac{1}{T}\int_0^T \frac{1}{\sqrt{4\pi t}} e^{-\frac{x^2}{4T}} dt \sim \frac{1}{\sqrt{\pi T}} e^{-\frac{x^2}{4T}} + O\left(erf\left(\frac{1}{\sqrt{T}}\right)\right) \tag{6.7}$$

To refine this calculation, one needs to take into account the background illumination and the saturation. The background illumination can be taken care of by subtracting the background image (the image when no molecule is present under the same visualization conditions). It is also necessary to set the contrast and acquisition times large enough to prevent saturation, or reduce the concentration of the fluorophores.

6.8 Measurement of temperature in a diffraction limited microscope

In a microscope setup, the camera's CCD is in the image plane of the microscope and coupled to the focus plane. Each pixel is coupled with a volume in the object plane that is related to the magnification of the microscope and to the depth of focus. This coupling affects signal to background ratio when measuring fine features as has been witnessed by single molecule experimentalists over the years. The intensity recorded by a single pixel is the convolution of the signal with the conjugate volume characteristic function resulting in an averaging of the signal over the conjugate volume. Additionally, on should add that the image is also a convolution with the point spread function (usually an Airy disk) of the setup which we ignore here.

$$\frac{I_{pixel}}{\overline{V}} = \iiint_{all\ space} s(\vec{r}) \times \chi_{\overline{V}}(\vec{r}) dV = \frac{1}{\overline{V}} \iiint_{\overline{V}} s(\vec{r}) dV \qquad (6.8)$$

In this equation $\overline{V}$ is the conjugate volume to the pixel, s is the signal, and $\chi_{\overline{V}}$ denotes the characteristic function of the conjugate volume.

FIGURE 6.4 Field of view-field of focus illustration

In our trapping setup, the effective size of the pixels is 8.47μm (H) x 6.6μm (V). The third dimension in the conjugate volume is the depth of field that is defined as the maximum axial separation of two points in focus at the same time. Several criteria have been adopted to determine this distance. The most commonly employed related the field of view d_{tot} of the objective to the numerical aperture NA, the immersion refractive index n, the magnification M, the wavelength λ, and the resolution e by the formula:

$$\frac{d_{tot}}{n} = \frac{\lambda}{NA^2} + \frac{e}{M \times NA} \tag{6.9}$$

For our setup with the 40x objective (Olympus LUCPlanFLN), we can take the depth of field to be 1μm consistently with the literature[51].

This eventually leads to a conjugate volume of dimensions 212nm (H) x 165nm (V) x 1.3μm (Z) in the object space for an effective pixel.

As a result, in a temperature measurement, the computed temperature in each pixel is the average of the temperatures over the conjugate volume. This is true because the temperature measurement is a linear operator between the intensity space and the temperature range.

$$T_{pixel} = T\left(E\left[I_{pixel}\right]\right) = E\left[T(I_{pixel})\right] = \frac{1}{V}\iiint_{\bar{V}} T(\vec{r})dV \tag{6.10}$$

From the heat simulations we can predict the temperature increase and compare the average temperatures to the measured temperatures.

CHAPTER 7

OPTO-MECHANICAL CHEMISTRY

The behaviour of molecules in solution is governed by energy barriers, potential wells, and stochastic events[1]. In particular, chemical reactions are often described in terms of a reaction energy diagram along a reaction coordinate. Electromagnetic potentials can add to these energy landscapes through their energy density without affecting other local potentials. Evanescent field can add energy barriers and potential wells that span only tens of nanometers[2] and have been used for the purpose of trapping molecules[3]. Doing so along a reaction coordinate would therefore modify the chemical reaction profoundly by favoring one reaction coordinate over another, and raising or lowering activation energies. Here we show that the adsorption reaction of proteins onto carbon nanotubes can be controlled with opto-mechanical forces. In the case of the adsorption reaction, the reaction coordinate is the distance from the molecule to the substrate, and the reaction energy diagram is modeled through the Derjaguin Landau Verwey Overbeek theory[4] and is then extended to account for the mechanical effects of the electromagnetic field. Experimentally, 1550nm laser light is delivered through silicon waveguides to multi-walled carbon nanotubes where the local electric field intensity is amplified because of their metallic structure. The adsorption of immunoglobulin proteins onto the nanotubes is shown to occur

only when the optical power is above a certain threshold, implying that the chemical reaction is opto-mechanically controlled. Our technique offers a new way to control molecules in chemical reactions that fundamentally differs from the current paradigms and is part of the emerging techniques allowing novel forms of interactions with molecules[5,6].

In energetic terms, reactions are described by energy diagrams that reflect the change in free energy along an abstractly defined reaction coordinate. Catalytic processes are aimed at changing this diagram by introducing a catalyst as a reaction intermediate that changes the reaction pathway[7]. Providing bulk energy to the reactants and deforming molecules through mechanical processes can also have a catalytic action while requiring specific molecular groups usually on polymers[8,9], mechanical processes have also been used to probe structures of molecules and bonds[10,11]. Light, and electro-magnetism in general, have also been used to provide energy to certain reactions[12] or even to dope catalysts[13] without requiring a physical presence in the solution. Very few methods can alter the energy reaction diagram without introducing a catalyst or providing energy as bulk kinetic energy, which either requires specific chemical groups[14] or can cause undesired reactions to also be accelerated[15] and eventually decrease the chemical efficiency.

In this work, we demonstrate a novel approach that uses light-mediated mechanical forces to locally modify the energy reaction diagram along the reaction coordinate. The technique relies on optical gradient forces acting on biomolecules in solution and on the adsorption of these molecules to hydrophobic surfaces. The exploitation of light to affect the motion of micrometer to nanometer scale particles was first pioneered by

Ashkin when he invented optical tweezers in 1986[16]. Since then, the optical gradient force has found numerous applications in physics[17] and biology[18]. Efforts to trap smaller molecules in solution have led to the recent development of molecular tweezers[19,20] which allows proteins to be trapped by nano-optics and nano-photonics structures.

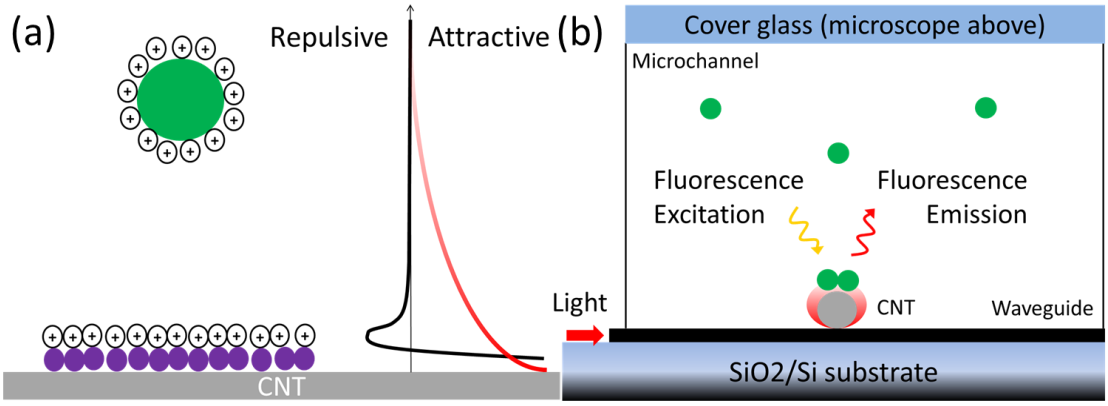

FIGURE 7.1. Schematics of the experiment and setup. (a) Application of an electromagnetic potential onto a spherical molecule to overcome the energy barrier in the energy reaction diagram. Black curve: reaction energy diagram. Red curve: optical potential. The large sphere represents the target molecule, the filled spheres represent molecules already at the surface of the substrate. Ions, here positive, are present at the surface of the molecules. (b) Schematic representation of the setup. The chip is composed a silicon waveguide on a 3 μm SiO2, 500 μm Si wafer. A microfluidic channel is mounted on top with parafilm walls and a coverslip on top. The setup is mounted on an upright microscope stage equipped with a low light camera.

The present demonstration of opto-mechanical chemistry modifies the adsorption of different forms of immunoglobulin proteins (Ig) to carbon nanotubes (CNTs). Multi-wall CNTs offer proteins a surface onto which they can adsorb when in sufficient proximity, and also exhibit metallic properties which can expand and enhance electromagnetic fields[21]. The reaction coordinate for the adsorption reaction is the distance between the two molecules, the same axis along which the optical gradient

force acts. The mechanical action of light enables the surface immobilization by helping the molecules overcome the energy barriers along the reaction pathway. In the absence of the light, the adsorption of the protein is prevented by double layer repulsion and by the presence of surfactant and blocking molecules at the surface of the CNTs. To our knowledge, this is the first demonstration of a bias of the reaction pathway along a controled reaction coordinate, it is achieved by providing energy to the reaction in the form of potential energy in contrast with other methods that provide kinetic energy to molecules[8].

The reaction diagram was analytically modeled with an extended Derjaguin-Landau-Verwey-Overbeek (DLVO) theory for simplicity, despite some of its known shortcomings[22]. The model equation (1) with its extension to include hydrophobic interactions between two hydrophobic molecules (a sphere and a cylinder) reads[23,24]:

$$U_{DLVO} = 64Rk_BTc_0\gamma_{0,p}\gamma_{0,CNT}{\lambda_D}^2 e^{-\frac{z}{\lambda_D}} - \frac{AR_p}{6z} - C_h e^{-\frac{z}{D_0}} \quad (1)$$

In this equation R is the gas constant, k_B is the Boltzmann constant, T is the temperature, c_0 is the bulk ionic concentration, λ_D is the Debye length calculated as $\lambda_D = \sqrt{\frac{RT\epsilon}{F^2 c_0}}$ where ε is the buffer permittivity and F is the Faraday constant, z is the distance between the molecules, A is the Hamaker constant, R_p is the radius of the protein, C_h and D_0 are parameters in the hydrophobic extension of the theory, and $\gamma_{0,p}$ and $\gamma_{0,CNT}$ are the surface charge densities of protein and CNTs respectively. A further assumption was used in this equation using the constant surface potential condition[25]. The DLVO theory was further extended in equation (2) to include the effects of the

surfactant molecule and the mechanical action of light. Along the reaction coordinate, the energy diagram now reads:

$$U = U_{DLVO} - \frac{\alpha}{L_{ev}}|E_0|^2 e^{-\frac{z}{L_{ev}}} + \Delta T \times S_T \times k_B T + N E_A \chi(z) \quad (2)$$

where α is the polarizability of the protein, L_{ev} is the evanescent field length, E_0 is the electromagnetic field strength, S_T is the Soret coefficient of the protein, N is the number of surfactant molecules that the protein needs to remove in order to dock on the nanotube, E_A is the activation energy required to remove the surfactant molecule, χ is a Heaviside step function supported where the surfactant molecule resides. The second term of the equation is the electromagnetic potential well arising from the gradient force, and the third term corresponds to the thermophoretic effect[26]. The last term is introduced here and intended to model the presence of surfactant and blocking buffer molecules at the nanotube surface which are used in both dispersing the nanotubes in solution and preventing non-specific adsorption.

Experimentally, a silicon waveguide is used to transport the 1550 nm laser light to the nanotube. The light from the waveguide evanescently couples to the carbon nanotubes where it is amplified. Similar schemes taking advantage of locally amplified light geometries have been used to trap nanoparticles and molecules[19,20]. In the present work, the resulting electromagnetic potential well along the reaction coordinate superimposes to the energy diagram and profoundly changes the chemical reaction as shown in Fig. 1a. A schematic view of the experimental setup is presented in Fig. 1b. The threshold power at which the adsorption starts is measured experimentally by observing the adsorption of the fluorescently tagged molecules and is taken to represent the height of the energy barrier in the DLVO theory. The opto-mechanical

adsorption of fluorescently tagged IgM proteins onto CNTs is presented in Fig. 2. Prior to each experiment, carbon nanotubes were first immobilized on the silicon waveguides and exposed to blocking buffer (StartingBlock TBS or SEA Block, Sigma Aldrich) for two hours. A dilution of 0.5 µg/ml of Alexa 488 conjugated IgM proteins in Phosphate Buffered Saline (0.1x PBS, 0.5% Tween 20) was prepared prior to each experiment. Time-lapse fluorescent images of the nanotubes in the IgM solution were captured in one minute intervals to slow bleaching. At the beginning of the experiment, no background fluorescence is visible indicating that few to no IgM molecule is adsorbed on the nanotube's surface as visible in Fig. 2a. The input laser power is increased by approximately 10 minutes steps and no adsorption is observed until it reaches the threshold power, as shown in Fig. 2a-d. The readout power of the 1550 nm light out of the chip is recorded at the output of the chip and the fluorescent intensity is recorded with a low light camera. The traces of the readout power and of the fluorescent signal are plotted in Fig. 2e as a function of time for two experiments in PBS 1X (brown and red) and two in PBS 0.1X (blue and navy). The colored dots represent the measured fluorescent intensity and the dashed lines are the power trace throughout the experiments. The steady state intensity, measured at the end of each power step, is also plotted in Fig. 2f as a function of the input power demonstrating that the adsorption only begins after the power reached a certain power threshold. The measured rate obtained from the steady states is also plotted in inset of Fig. 2f.

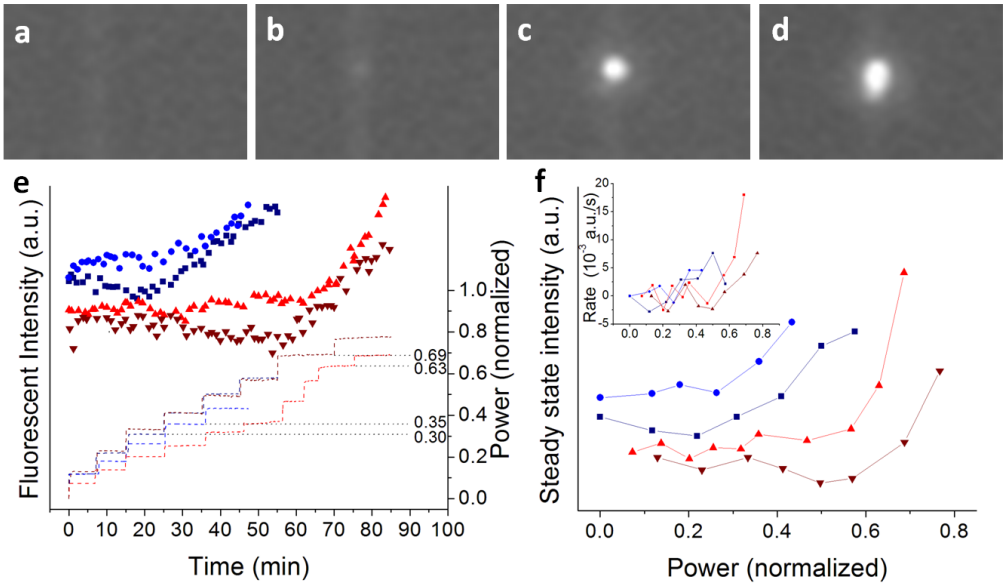

FIGURE 7.2. Aggregation of Alexa Fluor 488-conjugated immunoglobulins M on a nanotube observed under fluorescence microscopy. (a-d) Fluorescent images before (a) and after (b-d) reaching the power threshold for adorption. The bright spot is the aggregate. Each image is taken reaching steady state at the input power. (e) Plot of the measured fluorescent intensity for two data sets in PBS 0.1X (blue and navy dots) and two data sets in PBS 1X (red and brown dots). Dotted lines at the bottom correspond represent the normalized power output. (f) Plot of the steady state intensity as a function of coupled power for the same data sets as in (e). Inset: Rate of adsorption at each power step.

The measured threshold power depends on the coupling from the fiber to the waveguide and from the waveguide to the CNT which can vary from experiment to experiment. The measured powers are normalized by the power necessary to bring the temperature up from bulk temperature to boiling temperature because boiling always occurs at a given power density coupled in the carbon nanotube. Linearity of the heat and electromagnetic equations allow for such normalization. It therefore allows for direct comparison of experiments regardless of the coupling conditions.

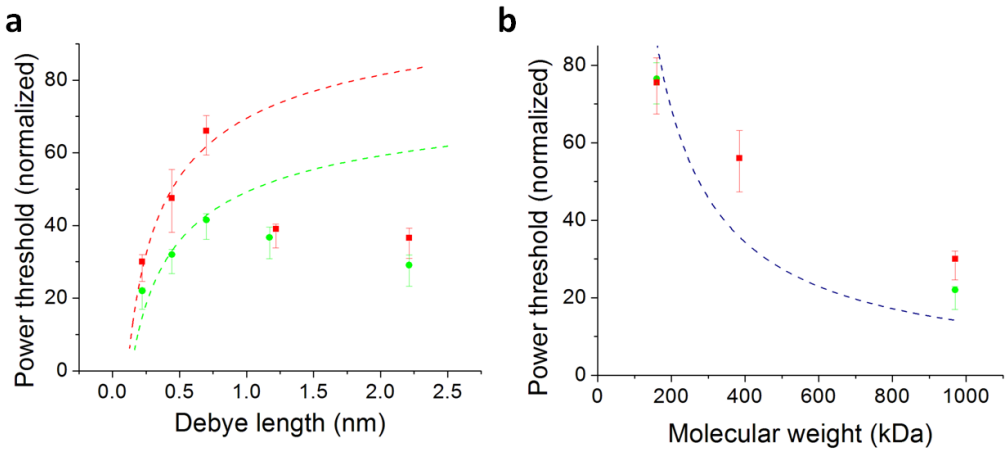

FIGURE 7.3. (a) Measured power threshold for accumulation as a function of the Debye length of the buffer (colored dots) and estimate of the energy barrier height from the DLVO model (dashed line). Qualitative agreement is observed for Debye lengths above 0.7 nm corresponding to PBS 1X and dilutions. Error bars account deviations in measurements and uncertainty related to the experimental method. (b) Measured power threshold for accumulation as a function of the molecular weight of the immunoglobulin species used (colored dots). The solid line presents the expected power threshold in the case where the potential barrier is the same across species. Error bars account for the dispersion of the measurements to which an additional 5% was added to account for the accuracy of the measurement method.

The effect of the Debye length in the buffer on the activation energy of the adsorption reaction was measured. The Debye length was manipulated through dilutions of the PBS buffer. The power threshold at which the adsorption begins was recorded and is plotted in Fig. 3a as a function of the Debye length of the buffer for experiments with two polarizations (green and red) along with the fitted activation energy as calculated from DLVO theory for different ionic strengths in solid curve. According to Equation (1), towards higher ionic strengths, or lower Debye lengths, the activation energy of the adsorption reaction should decrease due to dispersion forces. The necessary applied electromagnetic potential to overcome the activation energy and drive the reaction in Equation (2) should therefore decrease as well. Ignoring the effects of

thermophoresis, the input optical power threshold is expected to map the activation energy from Equation (1). The activation energy is in qualitative agreement with the DLVO model used here at low Debye lengths. Differences between the measured barrier height and the DLVO fit, particularly at higher Debye lengths, are attributed to the failure of the constant surface potential assumption and to changes in surface potential resulting from changes in pH[27]. The energy barrier was also measured for different immunoglobulin proteins as presented in Fig 3b. Equation (2) indicates that the potential well depth is proportional to the polarizability, α, of the molecule which in turn scales with the mass assuming a similar chemical composition. It is to be expected that more optical power is necessary to overcome the same potential barrier for proteins with lower molecular weights. Figure 3b presents the measured power threshold in PBS 10x for IgG, secretory IgA, and IgM with molecular weights 160 kDa, 385 kDa, and 970 kDa respectively. As expected, the necessary input power increases as the mass of the molecule decreases. The dashed curve presents the expected power threshold in the case where the potential barrier is the same across species.

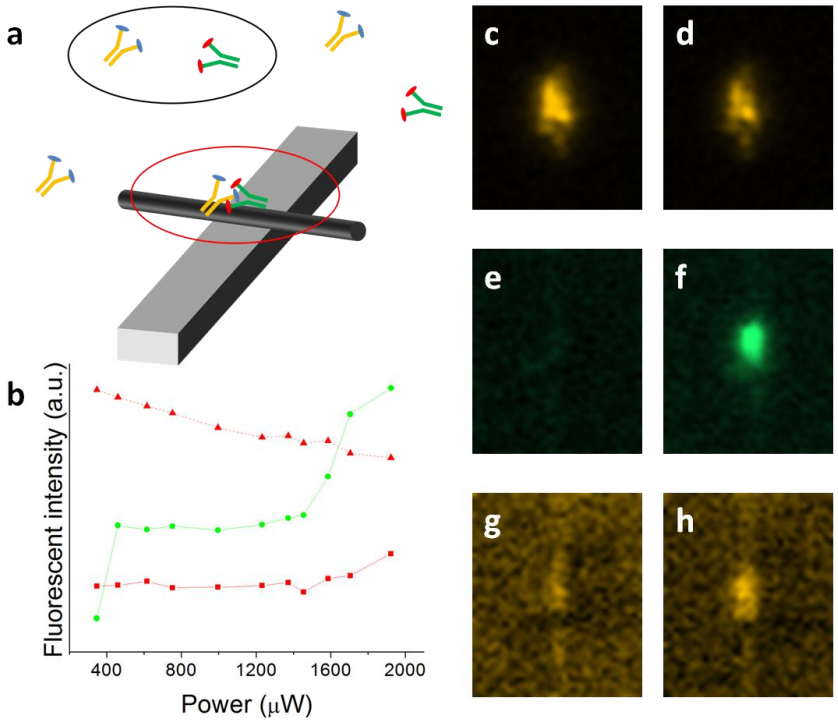

FIGURE 7.4. (a) The setup can also be used to drive reactions. Black circle: useful collisions in solutions are rare because of the low number of collisions and the relative speeds of the molecules. Green circle: in the potential well created by a metallic particle, trapped molecules are confined to a smaller region making rare processes more common and more observable. (c). Trace of the intensity of the acceptor (red triangles), donor (green circles), and FRET (red squares) fluorescent channels. The acceptor is seen to bleach while the donor and FRET remain unchanged until accumulation starts at which point the signals start. (c-h)) Pseudo-color contrast adjusted fluorescent images before (left column) and after (right column) accumulation started. (c,d) Acceptor channel, TRITC filter (e,f) Donor channel, FITC filter set (g,h) FRET channel, FRET filter set.

The electromagnetic potential was also used to drive a reaction between two mis-matched immunoglobulin proteins. By forcing the proximity between molecules, a Förster Resonance Energy Transfer (FRET) signal was obtained between a donor (Alexa Fluor 488, Life Technologies) and an acceptor (Tetramethylrhodamine isothiocyanate TRITC, Millipore) conjugated to a Goat Anti-Mouse IgM (Life Technologies) and a normal goat IgG (Millipore) respectively indicating that the

molecules were in a close proximity that cannot be achieved otherwise. By creating a high local concentration of molecules in close proximity, the corresponding increase in collisions can force reactions or other exchanges between molecules which are otherwise unlikely to occur[28] as illustrated in Fig. 4a. The acceptor molecule was first immobilized on the CNT as visible in Fig 4c and a blocking buffer (StartingBlock TBS, Sigma Aldrich) was used overnight. Little to no background is found for the donor and FRET filters as seen in Fig 4e,g (some background is due to the presence of the blocking buffer and Tween 20). When the optical trap is activated and the donor-conjugated IgM starts aggregating (as seen on Figure 4f), a FRET signal arises from the forced proximity between the donor fluorophores and the acceptor as visible in Fig 4h. The close proximity provided by this configuration augments the chances of energy transfer leading to FRET.

We demonstrated experimentally that optical gradient forces can alter chemical reactions by lowering selected energy barriers and affecting their energy pathways. They can also affect reactions by forcing proximity between molecules, as suggested by the FRET experiment, and could be made selective to molecular size or chirality. With other emerging methods, this work is part of the changing paradigm challenging established means of interaction with molecules[5,6]. This work opens a new venue towards catalysis and directed nano-assembly. It provides a way to interact with molecules that is entirely different to the methods currently used. It also offers a new approach to study molecular mechanics, to develop methods is surface sciences, to study reaction engineering in relation with molecular mechanics, and may provide

opportunities in studying structure-function relationship in large proteins or molecular clusters.

7.3 Methods

The silicon photonic waveguides were fabricated using standard Electron Beam lithography techniques at the Cornell Nanoscale Facility. A microfluidic channel consisting of a coverslip top, parafilm walls, and PDMS inlet/outlet was mounted on the chips prior to each experiment. Chips were cleaned overnight in Nanostrip (Cyantek) between experiments. The 1550 nm light from a tunable laser (ANDO AQ4321) was amplified (Amonics), delivered to the chip by a lensed fiber (OZ Optics), and brought to physical contact with the chip through end-fire coupling. The chip was mounted on a microscope stage equipped for bright field and epifluorescence (camera: Hamamatsu C4742-80-12AG). The CNT solutions were prepared by adding 5 mg of MWCNT (Sigma-Aldrich) and 0.5% Tween 20 (Sigma-Aldrich) to 10 mL heavy water and sonicating before each experiment for 20 minutes. Fresh dilutions of PBS (Sigma-Aldrich) were also sonicated with 0.5% Tween 20 for 10 minutes prior to each experiment, the pH was kept between 6.8 and 7.3 to optimize IgM integrity. Alexa Fluor 488-conjugated IgM (Life Technologies), TRITC-conjugated IgG (Millipore), and FITC-conjugated sIgA (Sigma-Aldrich), were diluted to 1 μg/ml in PBS before each experiment. After each experiment, the boiling power was measured in dark field microscopy and used to normalize each power curve.

7.4 Acknowledgments

We would like to thank Peng Chen and Alex Barbati for useful discussion on the modeling and Matthew Mancuso for his help in the FITC-conjugation of sIgA. This work was performed in part at the Cornell NanoScale Facility, a member of the National Nanotechnology Infrastructure Network, which is supported by the National Science Foundation (Grant ECS-0335765). The authors appreciate access and the use of the facilities of the Nanobiotechnology Center (NBTC), an STC Program of the National Science Foundation under Agreement No. ECS-9876771. This work was supported by the U.S. Department of Energy Office of Basic Science under Grant DE-SC0003935.

REFERENCES

1 Gardiner, C. W. *Handbook of stochastic methods*. Vol. 3 (Springer Berlin, 1985).

2 Jackson, J. D. & Fox, R. F. Classical electrodynamics. *American Journal of Physics* **67**, 841 (1999).

3 Yang, A. H. J. *et al.* Optical manipulation of nanoparticles and biomolecules in sub-wavelength slot waveguides. *Nature* **457**, 71-75, doi:10.1038/nature07593 (2009).

4 Norde, W. & Lyklema, J. Protein adsorption and bacterial adhesion to solid surfaces: A colloid-chemical approach. *Colloids and Surfaces* **38**, 1-13, doi:10.1016/0166-6622(89)80138-6 (1989).

5 Zhang, R. *et al.* Chemical mapping of a single molecule by plasmon-enhanced Raman scattering. *Nature* **498**, 82-86, doi:Doi 10.1038/Nature12151 (2013).

6 Takase, M. *et al.* Selection-rule breakdown in plasmon-induced electronic excitation of an isolated single-walled carbon nanotube. *Nat Photon* **7**, 550-554, doi:10.1038/nphoton.2013.129 (2013).

7 Chorkendorff, I. & Niemantsverdriet, J. W. *Concepts of modern catalysis and kinetics*. (Wiley-Vch, 2006).

8 Hickenboth, C. R. *et al.* Biasing reaction pathways with mechanical force. *Nature* **446**, 423-427 (2007).

9 Davis, D. A. *et al.* Force-induced activation of covalent bonds in mechanoresponsive polymeric materials. *Nature* **459**, 68-72, doi:10.1038/nature07970 (2009).

10 Rief, M., Oesterhelt, F., Heymann, B. & Gaub, H. E. Single molecule force spectroscopy on polysaccharides by atomic force microscopy. *Science* **275**, 1295-1297, doi:10.1126/science.275.5304.1295 (1997).

11 Merkel, R., Nassoy, P., Leung, A., Ritchie, K. & Evans, E. Energy landscapes of receptor-ligand bonds explored with dynamic force spectroscopy. *Nature* **397**, 50-53 (1999).

12 Fox, M. A. & Dulay, M. T. Heterogenous Photocatalysis. *Chem. Rev.* **93**, 341-357, doi:10.1021/cr00017a016 (1993).

13 Christopher, P., Xin, H. L. & Linic, S. Visible-light-enhanced catalytic oxidation reactions on plasmonic silver nanostructures. *Nature Chemistry* **3**, 467-472, doi:Doi 10.1038/Nchem.1032 (2011).

14 Beyer, M. K. & Clausen-Schaumann, H. Mechanochemistry: The mechanical activation of covalent bonds. *Chem. Rev.* **105**, 2921-2948, doi:10.1021/cr030697h (2005).

15 Drexler, K. E. Nanosystems- Molecular machinery, manufacturing, and computation(Book). *New York, NY: John Wiley & Sons, Inc, 1992.* (1992).

16 Ashkin, A., Dziedzic, J. M., Bjorkholm, J. E. & Chu, S. Observation of a Single-Beam Gradient Force Optical Trap for Dielectric Particles. *Optics Letters* **11**, 288-290 (1986).

17 Kippenberg, T. J. & Vahala, K. J. Cavity opto-mechanics. *Optics Express* **15**, 17172-17205, doi:Doi 10.1364/Oe.15.017172 (2007).

18 Block, S. M., Goldstein, L. S. B. & Schnapp, B. J. BEAD MOVEMENT BY SINGLE KINESIN MOLECULES STUDIED WITH OPTICAL TWEEZERS. *Nature* **348**, 348-352 (1990).

19 Pang, Y. & Gordon, R. Optical trapping of a single protein. *Nano Letters* **12**, 402-406 (2011).

20 Chen, Y.-F., Serey, X., Sarkar, R., Chen, P. & Erickson, D. Controlled photonic manipulation of proteins and other nanomaterials. *Nano Letters* **12**, 1633-1637 (2012).

21 Novotny, L. & Hecht, B. *Principles of nano-optics*. (Cambridge university press, 2006).

22 Boström, M., Williams, D. R. M. & Ninham, B. W. Specific Ion Effects: Why DLVO Theory Fails for Biology and Colloid Systems. *Phys. Rev. Lett.* **87**, 168103 (2001).

23 Israelachvili, J. & Pashley, R. The hydrophobic interaction is long range, decaying exponentially with distance. (1982).

24 Li, K. & Chen, Y. Evaluation of DLVO interaction between a sphere and a cylinder. *Colloids and Surfaces A: Physicochemical and Engineering Aspects* (2012).

25 Bhattacharjee, S. & Elimelech, M. Surface element integration: A novel technique for evaluation of DLVO interaction between a particle and a flat plate. *J Colloid Interf Sci* **193**, 273-285, doi:DOI 10.1006/jcis.1997.5076 (1997).

26 Serey, X., Mandal, S., Chen, Y.-F. & Erickson, D. DNA transport and delivery in thermal gradients near optofluidic resonators. *Phys. Rev. Lett.* **108**, 048102 (2012).

27 Stafiej, A. & Pyrzynska, K. Adsorption of heavy metal ions with carbon nanotubes. *Sep Purif Technol* **58**, 49-52, doi:DOI 10.1016/j.seppur.2007.07.008 (2007).

28 Shannon, R. J., Blitz, M. A., Goddard, A. & Heard, D. E. Accelerated chemistry in the reaction between the hydroxyl radical and methanol at interstellar temperatures facilitated by tunnelling. *Nat Chem* **advance online publication**, doi:10.1038/nchem.1692 (2013).

CHAPTER 8

CONCLUSIONS

8.1 Summary

In this thesis, I demonstrated a novel form of control of molecules in solution. The methods rely on nanophotonics and nano-optics. Using light fields tailored at the nanoscale, I developed a tool allowing for the manipulation of nanoscale objects and biomolecules.

Numerically, I found that photonic crystals could achieve record high trapping stiffness's in Chapter 2. Inserting a central hole allowed to increase the trapping stiffness for small molecules as they are now able to interact with the full field intensity. Photonic crystals were also used to exert an optical torque on nanorods in Chapter 3. In this case, the combination of the trapping force and the torque allowed for a control over five out of six degrees of freedom on the nano-object which illustrate the tremendous level of control that photonics can exert on nano-objects.

Realizing that water absorption in the near Infra Red would lead to significant heat, I characterized the heat produced by a photonic crystal resonator and studied its effect on molecular transport in chapter 4. I found that the heat generated could be very significant and could have major impacts on the operation of nanophotonic traps and bio-sensors. It could denature molecules that are sensitive to temperature. It could also affect the transport of the molecules from the bulk solution to the region of interest.

In chapter 6, I proposed and demonstrated a new application to the manipulation of molecules with nanophotonic tweezers: the manipulation of chemical reactions through electromagnetic potentials. I demonstrated that optical trapping forces could help immunoglobulin proteins to overcome activation energies in their path to adsorbing onto carbon nanotubes.

8.2 Engineering Better Traps

It is possible to engineer electromagnetic fields with extremely high k vector components along one direction. In real space, this means that it is possible to manufacture electromagnetic fields decaying over extremely short distances, and therefore engineer extremely high forces on molecules. Given that the optical trapping force is proportional to the gradient of the optical field, this would lead to extremely high trapping forces. For this reason, I am convinced that it is possible to trap molecules of sizes down to a few thousands of Daltons (at which point the contrast between the polarization of the molecule and that of the surrounding medium would lead to unexplored physics).

Not only would these traps allow manipulating smaller molecules, or larger molecules with smaller power consumption, but extremely localized fields could act only parts of a molecule.

As demonstrated in chapter 4, the other consideration in engineering better optical traps is the minimization of heat production, and the optimization of molecular transport. In the context of plasmonics, it has been shown that including a heat sink that lowers the temperature increase by 100-fold[18]. Realizing that relying on

convection rather than diffusion for the delivery of the solutes, researchers have proposed a solution to the delivery problem by forcing the fluid flow towards the optical element[51].

An important challenge remains untouched: the parallelization of optical trapping to large number of molecules. The power requirements for manipulating small molecules remain too high in the current methods for them to be scalable. Other engineering or physical solutions will need to be devised to address this challenge.

8.3 The case for photonic-plasmonic hybrids

The requirement for shorter field decay lengths is more structured materials. Structuring refractive indices without metals at the nanoscale is difficult because it usually relies on etching dielectrics which is extremely difficult when the desired precision is down to a few nanometers. An easier task is the deposition of materials, numerous methods have been developed to deposit metals with high degrees of accuracy and are already used to fabricate plasmonic devices[52]. Photonics, offer confined fields and evanescent excitations that are useful in plasmonics, are integrated in chips. Together, they allow for an enhancement of the light matter interaction. The field has recently attracted a large number of optics researchers. The work in opto-mechanical chemistry uses such hybrids because the carbon nanotubes have a metallic structure. To the best of my knowledge this is the first use of such hybrids in trapping.

I propose in APPENDIX B a possible design for improving our optical traps. It relies on deposited metals on a silicon nitride waveguide.

This type of designs offers several important advantages:

1- They allow for the optical engineering of the hybrid optimized for obtaining high trapping forces. The highly successful bowtie antenna, for example, could be implemented on the waveguide.
2- The metallic particles on the waveguides can be connected to metallic heat sinks that allow for the reduction of temperature by several orders of magnitude.
3- They offer a more controllable environment than the use of the self assembled carbon nanotubes traps where the angle od docking of the CNT and their somewhat disparate properties are sources of noise in measurements.

I propose in APPENDIX B a different possible design based on these considerations.

8.4 Possible Future Direction

When developing these methods, one of our main objectives has been to develop a toolset available to all engineers to approach molecules the same way one would approach macroscopic objects. This represents a shift from the traditional top-down, bottom-up paradigms in nanotechnology. In situ methods such as the ones developed here may help in nano-assembly.

The mechanical manipulation of molecules is part of an emerging new paradigm allowing new approaches to chemistry. The manipulation of chemical reactions is one example of what is doable when in control of molecules. Other applications remain to be developed.

Among the most exciting possible applications of molecular tweezers in scientific studies, the following seem particularly interesting in my opinion:

1- Observing dynamics of one, or two trapped molecules.
2- Obtaining spectroscopic signatures from trapped single molecules, and eventually identifying single molecules in solution.
3- Studying the effects of mechanical deformation on the activity of biomolecules.
4- Altering reaction pathways and protein folding with optical forces.
5- Mechanically immobilizing molecules to their lowest translational and rotational states.

APPENDIX A. FABRICATION SCHEMATICS FOR AN ON-CHIP SILICON PHOTONIC CRYSTAL RESONATOR FROM AN SOI WAFER

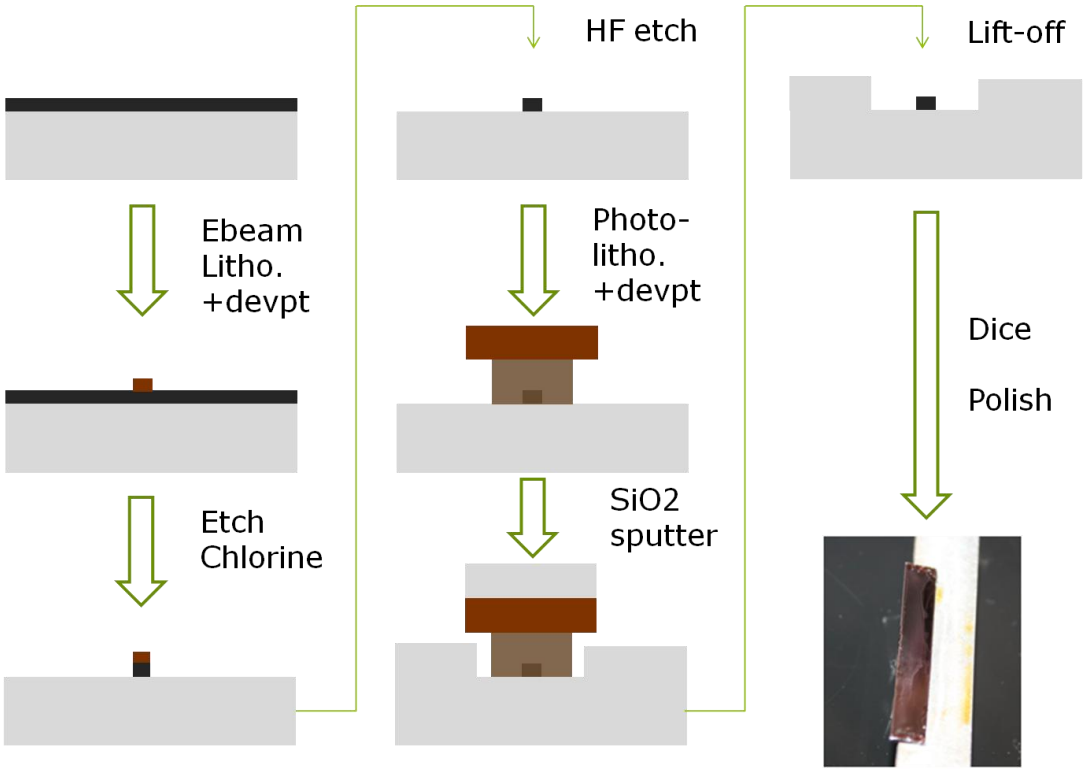

FIGURE A.1 Fabrication schematics. The photonic crystal resonator was fabricated on a 250 nm silicon-on-insulator wafer with 3 microns of buried oxide. The waveguides and resonators were patterned with Electron Beam lithography using the JEOL 9300 and an oxide resist (XR-1541), and the silicon was etched with a chlorine recipe in the Plasma Therm 770 (left chamber). Last, 2 to 3 microns of silicon oxide layer were sputtered (lift-off process) on the non-optofluidic components of the chip to protect the chip and reduce transmission losses.

APPENDIX B. PROPOSED IMPROVEMENT FOR TRAPPING SMALLER MOLECULES WITH LESS HEAT GENERATION.

Plasmonic-photonic hybrids have proven very efficient in producing traps for molecules. The use of carbon nanotubes on waveguides permitted the trapping of proteins of sizes going down to 160 kDa but produced significant heat. To trap 160 kDa molecules, the optical power used was also generating a 70K temperature increase incompatible with biology. Trapping smaller molecules should be possible with the same scheme but requires even more power, and therefore more heat. Depositing metals in place of metallic nanotubes would provide two major benefits.

1) The size, shape, and coupling of the metallic structure can be controlled more accurately and more consistently which would diminish some of the noise in measurements observed in the chapter “Opto-Mechanical Chemistry”.
2) The plasmonic particle can be connected to a heat sink dimishing the temperature rise by up to two orders of magnitude[18]. With a polarization scaling linearly with mass, this would allow for the trapping of down to 1.6 kDa before reaching 70 K temperature increase making the technique compatible with most biomolecules.

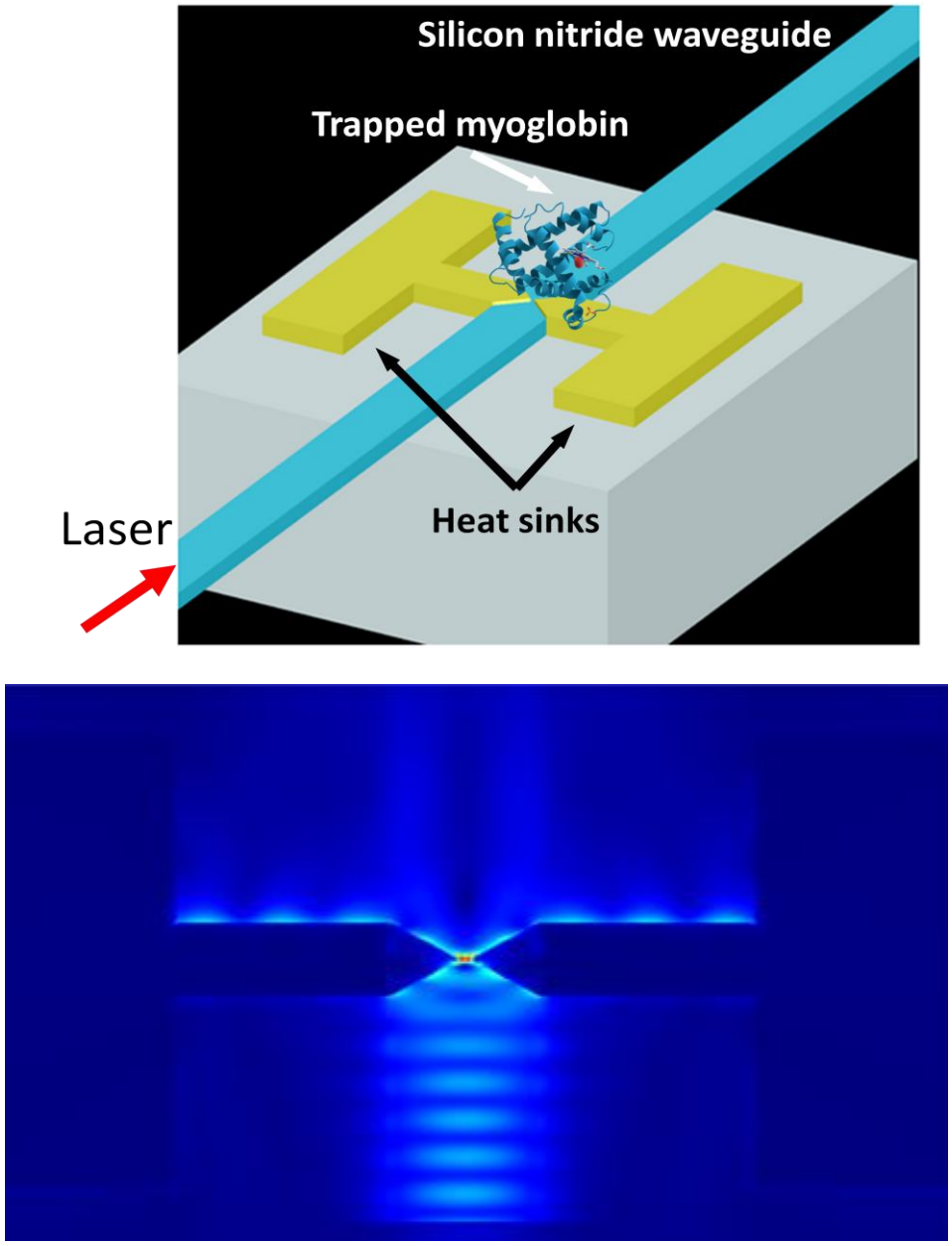

FIGURE B1. Possbile design for a plasmonic-photonic hybrid with a heat sink. The gray region represents the silicon dioxide substrate. The blue beam stripe is the silicon nitride resonator waveguide. The yellow region represents a metallic (Au, Ag) bowtie antenna deposited on top of the waveguide and the heat sink on the sides.

REFERENCES

1. Williams, D.B. and C.B. Carter, *The Transmission Electron Microscope*. 1996: Springer.
2. Kneipp, K., et al., *Single molecule detection using surface-enhanced Raman scattering (SERS).* Physical Review Letters, 1997. **78**(9): p. 1667.
3. Cui, X., et al., *Reproducible measurement of single-molecule conductivity.* Science, 2001. **294**(5542): p. 571-574.
4. Anger, P., P. Bharadwaj, and L. Novotny, *Enhancement and quenching of single-molecule fluorescence.* Physical Review Letters, 2006. **96**(11): p. 113002.
5. Rief, M., et al., *Single molecule force spectroscopy on polysaccharides by atomic force microscopy.* Science, 1997. **275**(5304): p. 1295-1297.
6. Smith, S.B., Y. Cui, and C. Bustamante, *Overstretching B-DNA: the elastic response of individual double-stranded and single-stranded DNA molecules.* Science, 1996. **271**(5250): p. 795-799.
7. Stipe, B., M. Rezaei, and W. Ho, *Single-molecule vibrational spectroscopy and microscopy.* Science, 1998. **280**(5370): p. 1732-1735.
8. Lu, H.P., L. Xun, and X.S. Xie, *Single-molecule enzymatic dynamics.* Science, 1998. **282**(5395): p. 1877-1882.
9. Jain, P.K., et al., *Near-field manipulation of spectroscopic selection rules on the nanoscale.* Proceedings of the National Academy of Sciences, 2012. **109**(21): p. 8016-8019.

10. Takase, M., et al., *Selection-rule breakdown in plasmon-induced electronic excitation of an isolated single-walled carbon nanotube.* Nat Photon, 2013. **7**(7): p. 550-554.

11. Zhang, R., et al., *Chemical mapping of a single molecule by plasmon-enhanced Raman scattering.* Nature, 2013. **498**(7452): p. 82-86.

12. Novotny, L. and B. Hecht, *Principles of nano-optics*. 2012: Cambridge university press.

13. Chen, Y.-F., et al., *Controlled photonic manipulation of proteins and other nanomaterials.* Nano Letters, 2012. **12**(3): p. 1633-1637.

14. Mandal, S., X. Serey, and D. Erickson, *Nanomanipulation Using Silicon Photonic Crystal Resonators.* Nano Letters, 2010. **10**(1): p. 99-104.

15. Hunt, H.K. and A.M. Armani, *Label-free biological and chemical sensors.* Nanoscale, 2010. **2**(9): p. 1544-1559.

16. Erickson, D., et al., *Review: Nanomanipulation using Near Field Photonics.* Lab on a chip, 2011. **11**(6): p. 995-1009.

17. Yang, A.H.J., et al., *Optical manipulation of nanoparticles and biomolecules in sub-wavelength slot waveguides.* Nature, 2009. **457**(7225): p. 71-75.

18. Wang, K., et al., *Trapping and rotating nanoparticles using a plasmonic nano-tweezer with an integrated heat sink.* Nature Communications, 2011. **2**: p. 469.

19. Ashkin, A., J.M. Dziedzic, and T. Yamane, *Optical Trapping and Manipulation of Single Cells Using Infrared-Laser Beams.* Nature, 1987. **330**(6150): p. 769-771.

20. Ashkin, A. and J.M. Dziedzic, *OPTICAL TRAPPING AND MANIPULATION OF VIRUSES AND BACTERIA.* Science, 1987. **235**(4795): p. 1517-1520.

21. Ashkin, A., *Acceleration and Trapping of Particles by Radiation Pressure.* Physical Review Letters, 1970. **24**(4): p. 156-159.

22. Miller, R.D. and T.B. Jones, *Electro-Orientation of Ellipsoidal Erythrocytes - Theory and Experiment.* Biophysical Journal, 1993. **64**(5): p. 1588-1595.

23. Allen, L., et al., *Orbital Angular-Momentum of Light and the Transformation of Laguerre-Gaussian Laser Modes.* Physical Review A, 1992. **45**(11): p. 8185-8189.

24. Friese, M.E.J., et al., *Optical angular-momentum transfer to trapped absorbing particles.* Physical Review A, 1996. **54**(2): p. 1593-1596.

25. He, H., et al., *Direct Observation of Transfer of Angular-Momentum to Absorptive Particles from a Laser-Beam with a Phase Singularity.* Physical Review Letters, 1995. **75**(5): p. 826-829.

26. Vogel, R., et al., *Synthesis and Surface Modification of Birefringent Vaterite Microspheres.* Langmuir, 2009. **25**(19): p. 11672-11679.

27. Padgett, M. and R. Bowman, *Tweezers with a twist.* Nature Photonics, 2011. **5**(6): p. 343-348.

28. Dholakia, K. and T. Cizmar, *Shaping the future of manipulation.* Nature Photonics, 2011. **5**(6): p. 335-342.

29. La Porta, A. and M.D. Wang, *Optical torque wrench: Angular trapping, rotation, and torque detection of quartz microparticles.* Physical Review Letters, 2004. **92**(19).

30. Schneider, C.A., W.S. Rasband, and K.W. Eliceiri, *NIH Image to ImageJ: 25 years of image analysis.* Nature Methods, 2012. **9**(7): p. 671-675.

31. Erickson, D., et al., *Nanomanipulation using near field photonics.* Lab on a Chip, 2011. **11**(6): p. 995-1009.

32. Chen, Y.F., et al., *Controlled Photonic Manipulation of Proteins and Other Nanomaterials.* Nano Letters, 2012. **12**(3): p. 1633-1637.

33. Lin, S.Y., E. Schonbrun, and K. Crozier, *Optical Manipulation with Planar Silicon Microring Resonators.* Nano Letters, 2010. **10**(7): p. 2408-2411.

34. Juan, M.L., et al., *Self-induced back-action optical trapping of dielectric nanoparticles.* Nat Phys, 2009. **5**(12): p. 915-919.

35. Wang, K., et al., *Trapping and rotating nanoparticles using a plasmonic nano-tweezer with an integrated heat sink.* Nat Commun, 2011. **2**: p. 469.

36. Liu, M., et al., *Light-driven nanoscale plasmonic motors.* Nat Nano, 2010. **5**(8): p. 570-573.

37. Serey, X., S. Mandal, and D. Erickson, *Comparison of silicon photonic crystal resonator designs for optical trapping of nanomaterials.* Nanotechnology, 2010. **21**(30).

38. Serey, X., et al., *DNA Transport and Delivery in Thermal Gradients near Optofluidic Resonators.* Physical Review Letters, 2012. **108**(4).

39. Tong, L., V.D. Miljković, and M. Käll, *Alignment, Rotation, and Spinning of Single Plasmonic Nanoparticles and Nanowires Using Polarization Dependent Optical Forces.* Nano Letters, 2009. **10**(1): p. 268-273.

40. Han, Y., et al., *Brownian motion of an ellipsoid.* Science, 2006. **314**(5799): p. 626-630.

41. Minoura, I. and E. Muto, *Dielectric measurement of individual microtubules using the electroorientation method.* Biophysical Journal, 2006. **90**(10): p. 3739-3748.

42. Cai, H. and A.W. Poon, *Planar optical tweezers using tapered-waveguide junctions.* Optics Letters, 2012. **37**(14): p. 3000-3002.

43. Schneider, T.M., S. Mandre, and M.P. Brenner, *Algorithm for a Microfluidic Assembly Line.* Physical Review Letters, 2011. **106**(9): p. 094503.

44. Almeida, V.R., R.R. Panepucci, and M. Lipson, *Nanotaper for compact mode conversion.* Optics Letters, 2003. **28**(15): p. 1302-1304.

45. Samy, R., T. Glawdel, and C.L. Ren, *Method for Microfluidic Whole-Chip Temperature Measurement Using Thin-Film Poly(dimethylsiloxane)/Rhodamine B.* Analytical Chemistry, 2007. **80**(2): p. 369-375.

46. Kellner, L., *The Near Infra-Red Absorption Spectrum of Heavy Water.* P ROY SOC LOND A MAT, 1937. **159**(898): p. 410-415.

47. Gray, D.D. and A. Giorgini, *VALIDITY OF BOUSSINESQ APPROXIMATION FOR LIQUIDS AND GASES.* International Journal of Heat and Mass Transfer, 1976. **19**(5): p. 545-551.

48. Donner, J.S., et al., *Plasmon-Assisted Optofluidics.* ACS Nano, 2011: p. Online Publication.

49. Duhr, S. and D. Braun, *Why molecules move along a temperature gradient.* Proceedings of the National Academy of Sciences of the United States of America, 2006. **103**(52): p. 19678-19682.

50. Duhr, S. and D. Braun, *Thermophoretic Depletion Follows Boltzmann Distribution.* Physical Review Letters, 2006. **96**(16): p. 168301.

51. Liu, X.Y., W.H. Wang, and Y. Sun, *Dynamic evaluation of autofocusing for automated microscopic analysis of blood smear and pap smear.* Journal of Microscopy-Oxford, 2007. **227**(1): p. 15-23.

52. Huang, M., et al., *Reusable Nanostencils for Creating Multiple Biofunctional Molecular Nanopatterns on Polymer Substrate.* Nano Letters, 2012. **12**(9): p. 4817-4822.